# Journal Of Semiconductor Science And Technology

**Volume No. 13**

**Issue No. 1**

**January - April 2025**

**ENRICHED PUBLICATIONS PVT.LTD**

**JE - 18,Gupta Colony, Khirki Extn,**
**Malviya Nagar, New Delhi - 110017.**
**E- Mail: info@enrichedpublication.com**
**Phone :- +91-8877340707**

# Journal Of Semiconductor Science And Technology

## Aims and Scope

Journal of Semiconductor Science & Technology is a journal of high quality devoted to the publication of original research papers on all aspects of semiconductor research and applications. The journal publishes original research papers on main aspects of experimental and theoretical studies of the properties of semiconductors and their interfaces. Appropriate subjects include but not limited to electrical properties, optical properties, device design, device fabrication, materials processing, materials and device analysis, process monitoring, reliability. Review articles in selected areas are published from time to time.

# Journal Of Semiconductor Science And Technology

# Journal Of Semiconductor Science And Technology

(Volume No. 13, Issue No. 1, January - April 2025)

## Contents

# The electrical switching properties of $Ge_{10}Se_5Sb_{85}$ chalcogenide glass

S. Abouelhassan
*Physics Department, Faculty of Science*
*Jazan University, KSA*

## A B S T R A C T

Bulk ingot material of the ternary mixture $Ge_{10}Se_5Sb_{85}$ was prepared by direct fusion of high purity constituent elements in vacuum sealed silica tube. The glassy nature of the prepared sample was confirmed by the X-ray diffraction (XRD) technique. Current -Voltage characteristics of the investigated glass have been carried out at different thicknesses and temperatures. Switching phenomenon at the turn-over point (TOP) from a high-resistance state (OFF state) to a negative-differential resistance-state (NDRS) was detected where the threshold parameters such as threshold dissipated power ($P_{th}$) ,threshold voltage( $V_{th}$),threshold current ($I_{th}$),threshold electric field ($E_{th}$) and threshold resistance ($R_{th}$)were determined at different thicknesses and ambient temperatures of the investigated samples. At the turn-over point ,the activation energies ($\Delta E_p$, $\Delta E_v$, $\Delta E_i$ ,$\Delta E_r$ and $\Delta E_f$) caused by the threshold dissipated powers, threshold voltages, threshold currents, threshold resistances and threshold electric fields respectively, were deduced at different thicknesses of the samples. The increasing in the ambient temperature of the investigated material ($\Delta T_J$), the temperature of the conduction path ($T^{\backslash}$ ) and the Poole-Frenkel coefficient ($\beta_{PF}$) were determined at different ambient temperatures and thicknesses of the samples on the basis of the Joule heating effects. The activation energy of hopping (W), the activation energy of conduction $\Delta E_\sigma$(eV), the hopping distance (d) of the charge carriers and the density of localized states N(E) were carried out due to Poole-Frenkel effect.

Keywords : Switching, chalcogenide, glass, Poole-Frenkel effect.

PACS Nos.: 71.23An,71.23Cq,61.82Fk,31.43.Fs

## 1. INTRODUCTION

One of the most important class of glass is the chalcogenide glass. It contains at least one of the chalcogen elements; sulfur, selenium or tellurium, and is of essential interest owing to their wide application in optoelectronics, electrical and optical memory devices, modern electronics, and solar cells. Chalcogenide glass has attracted great attention because of their interesting semiconducting properties[1,2] that can be used in various solid state-devices, such as power control and information storage devices and also because of their more recent importance in optical recording[3]. They are considered as core materials for optical fibers for light transmission, particularly when small lengths and flexibility are required. Binary and ternary chalcogenide glasses exhibit many useful properties including, particularly, the switching phenomenon. In chalcogenide glass there exists two types of switching which are threshold and memory switching based on the way the glasses respond to the removal of the electric field after the switching event[4-12]. In the first type of switching, the ON state can be observed only when a current flows down to a certain holding voltage, while in the memory type one, the ON state is permanent until a suitable reset current pulse is applied on the sample[13]. The investigated glasses are important due to their interesting optical properties for their potential use as optical fibers, and electrical memory devices. The phenomenon of electrical switching in this type of glass has attracted several technological applications including power control and information storage.

In threshold-type switching, no structural changes occur and the process could be considered as reversible, whereas in memory-type switching, the material undergoes significant structural changes after transition and the process becomes completely irreversible[14,15]. The sudden change in the electrical resistance of chalcogenide glasses from a low conducting "OFF" state to a high conducting "ON" state under the effect of an appropriate electric field is commonly referred to as the switching/threshold electric field[16]. The switching process consists of a change of several orders of magnitude in electrical resistance caused by the application of a voltage higher than a critical voltage known as the threshold or switching voltage($v_{th}$), which corresponds to the threshold resistance ($R_{th}$), threshold current ($I_{th}$), threshold dissipated power ($P_{th}$) , and threshold electric field ($E_{th}$) . The application of a high electric field across high-resistivity materials sometimes results in either switching to a low-resistance state or entering a region of current- controlled negative resistance (CCNR)[17]. On the removal of the excitation electric field, threshold switching glasses revert to the OFF state whereas memory switches remain locked to the ON state[18]. Memory switches originate from the boundaries of the glass-forming regions, where glasses tend to crystallize when heated or cooled slowly[19-21]. There are several models proposed to understand the memory and threshold types of electrical switching, which are exhibited by the chalcogenide glasses. They have been classified into purely electronic[22], thermal and electrothermal models[23-27]. The electronic mechanism appears to govern thin films, while the electrothermal model appears to control the bulk specimens[28] and some investigators[23,29,30] have considered the threshold switching as an electronic process. Investigations on the current-voltage characteristics and some studies on the dependence of the switching voltage and current on different material properties, such as composition, thickness, and pressure, will help investigators to understand the conduction mechanisms of the chalcogenide glasses. In the present work, the effect of thickness and temperature on the I-V characteristics and some switching parameters of $Ge_{10}Se_5Sb_{85}$ chalcogenide glasses will be investigate.

## 2. MATERIAL AND METHODS

Bulk chalcogenide glasses of $Ge_{10}Se_5Sb_{85}$ were prepared using the conventional melt quenching technique. Elemental constituents of 5N purity were weighed according to their atomic percentages and sealed in evacuated ($10^{-5}$ Torr) silica tubes then heated gradually to 1223 K for 15 h. The melt was continuously stirred to ensure homogeneity and then rapidly quenched in ice water. The glassy nature of the prepared samples was confirmed by the X-ray diffraction (XRD) technique using a Shimadzu XD-3 diffractometer with scanning velocity of 20 scans/min and Cu foil as the radiation source. Current–voltage characteristics were analyzed point by point using two electrometers (Keithley 617C). The glass samples were sandwiched between two electrodes, one of which was a pin electrode. The best fit for the resultant data points was made using the least- square method.

## 3. RESULTS AD DISCUSSION

### 3.1. Temperature dependence of the I -V characteris tics of $Ge_{10}Se_5Sb_{85}$

Current-voltage(I-V) characteristics and switching phenomena of different thicknesses of amorphous $Ge_{10}Se_5Sb_{85}$ at different ambient temperatures are given in Figs. 1a-1d.

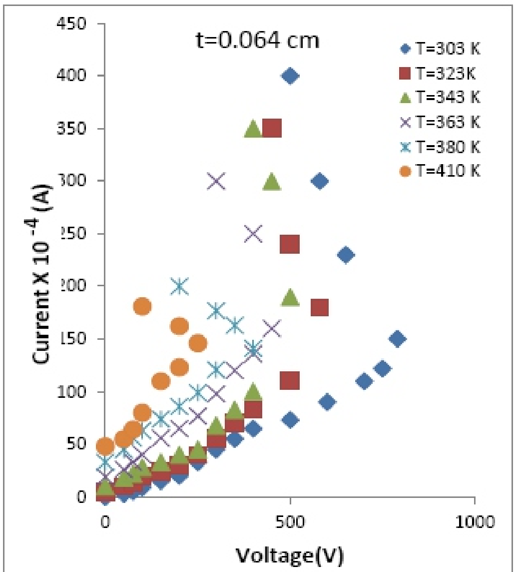

Figure:1a

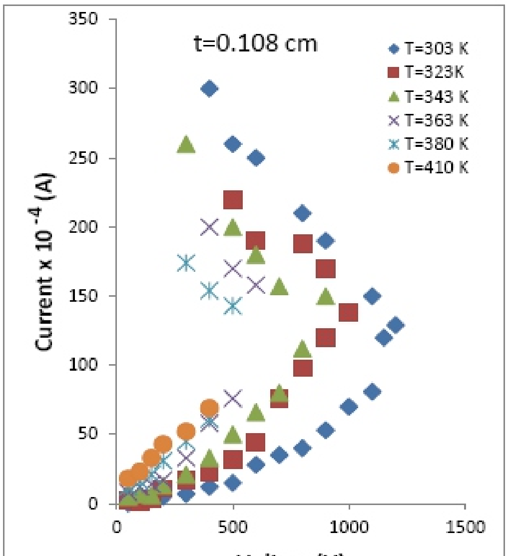

Figure:1b

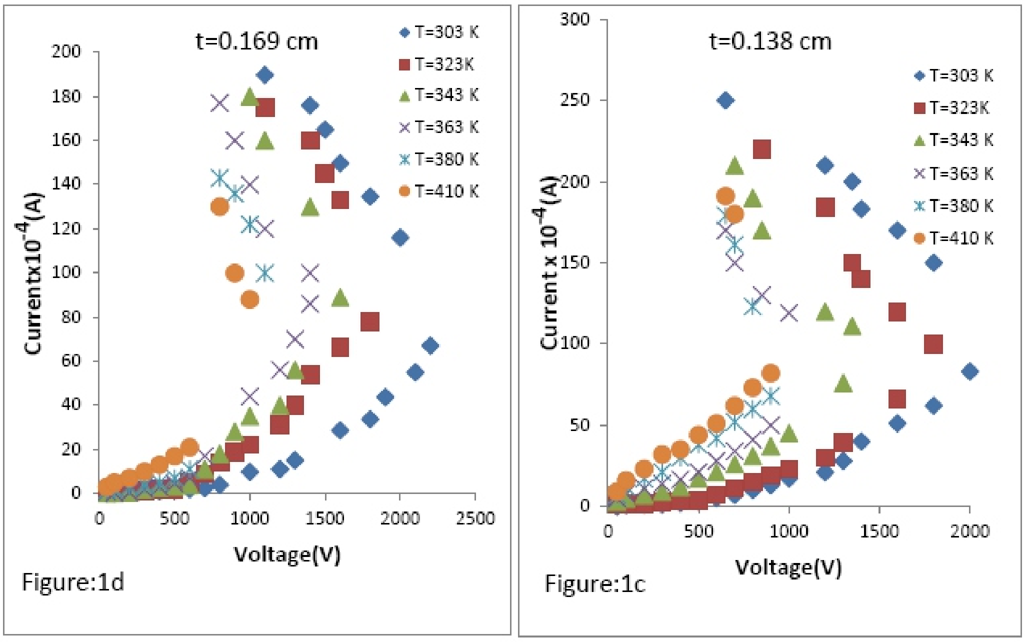


FIG. 1a -1d. The I-V characteristics of different thicknesses(t=0.064 cm, t=0.108 cm, t=0.138 cm and t=0.169 cm) for the glassy sample $Ge_5Se_{15}$ $Sb_{85}$ at different ambient temperatures.

From the figures it can be noticed that the sample exhibit an Ohmic behavior at lower applied voltages which is characterized by the high resistance state(OFF state). The OFF state region ,for the investigated samples(t=0.064 cm as a representative sample) can be redrawn, as shown in Figs. 2a-2d,

where it can be observed that, as the voltage across the sample increases , then the current increase linearly (Ohmic behavior), forming the first region (o-a) in the OFF state, which represents the high-resistance state.

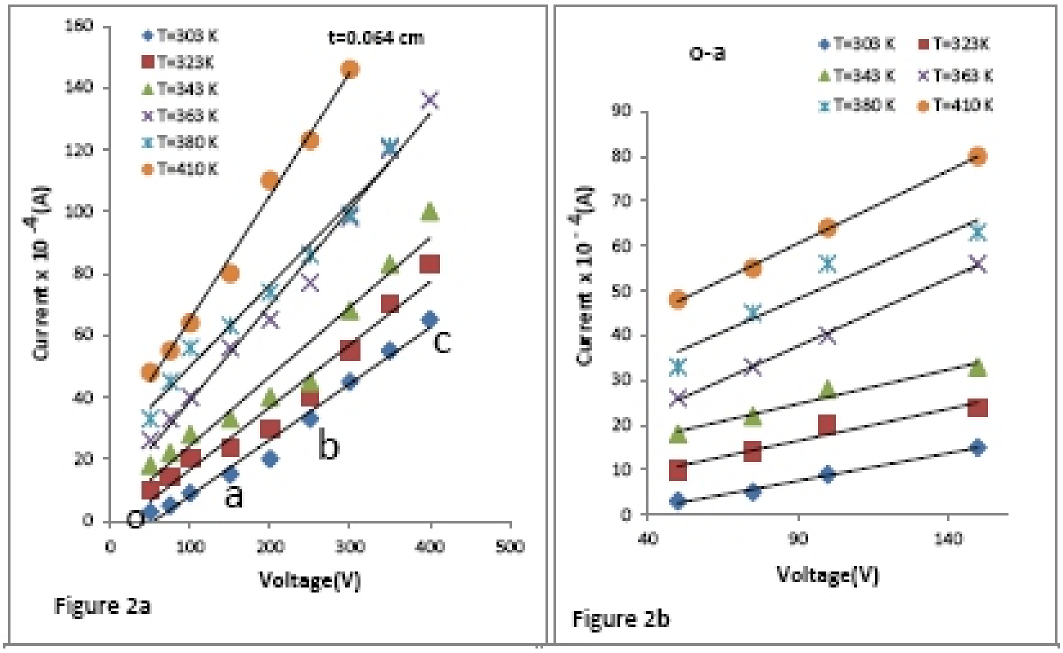

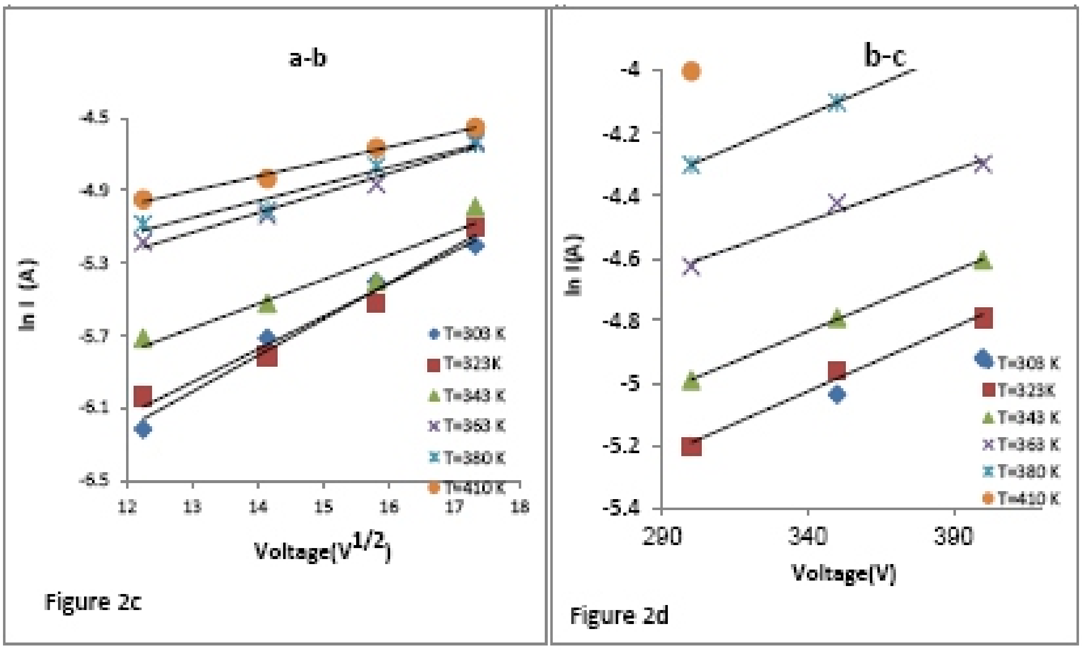


FIG. 2a -2d. The I-V Characteristics of the sample(t=0.064 cm) at different ambient temperatures in the OFF state.

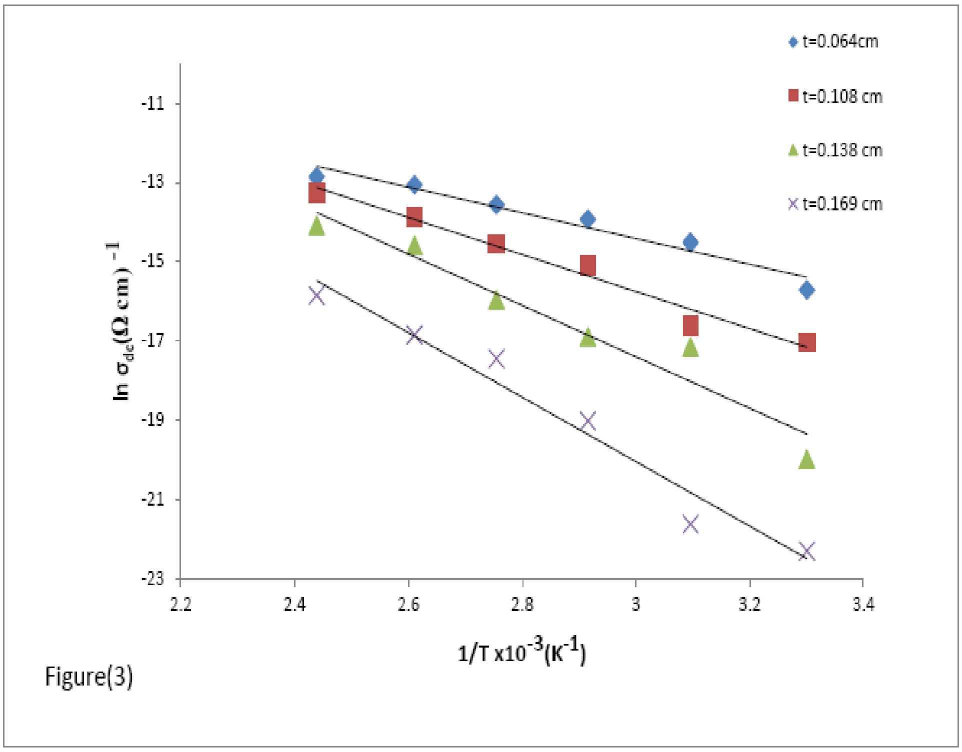


FIG. 3 . The temperature dependence of the dc conductivity of $Ge_{10}$ $Se_5$ $Sb_{85}$ at different ambient temperatures.

The dc conductivity of the investigated samples was plotted(as shown in Fig. 3) against the ambient temperature, at different thickness, according to the relation:

$$\sigma_{dc} = \sigma_o \exp(-\Delta E_\sigma / k_B T) \quad (1)$$

Where $\Delta E_\sigma$ is the activation energy of conduction. The deduced values of $\Delta E_\sigma$ at different thickness of the investigated samples are given in Table 2 where it can be noticed that as the sample thickness increases, the conductivity decreases which may be attributed to the increase in the disorder scattering process of the charge carriers which leads to increase the activation energy of conduction with the sample thickness as given in Table 2 and Fig. 9.

Table(1): The obtained values of the rise in the ambient temperature of the material($\Delta T_J$), temperature of the conduction path($T^{\backslash}$ ) and the Poole - Frenkel coefficient($\beta_{PF}$) at different temperatures and thicknesses of $Ge_{10}Se_5Sb_{85}$

| | t=0.064cm | | | t=0.108 cm | | | t=0.138 cm | | | t=0.169 cm | | |
|---|---|---|---|---|---|---|---|---|---|---|---|---|
| Temperature (K) | $N(E_F)$ ($10^{15}eV^{-1}cm^{-3}$) | d ($10^{-6}$ m) | W(eV) | $N(E_F)$ ($10^{16}eV^{-1}cm^{-3}$) | d ($10^{-6}$cm) | W(eV) | $N(E_F)$ ($10^{16}eV^{-1}cm^{-3}$) | d ($10^{-6}$ cm) | W(eV) | $N(E_F)$ ($10^{16}eV^{-1}cm^{-3}$) | d ($10^{-6}$ cm) | W(eV) |
| 303 | 0.78 | 6.46 | 1.126 | 4.2 | 4.23 | 0.737 | 10.9 | 3.34 | 0.582 | 14.5 | 3.11 | 0.543 |
| 323 | 2.99 | 4.55 | 0.845 | 8.5 | 4.10 | 0.762 | 11.7 | 3.23 | 0.601 | 16.2 | 2.98 | 0.554 |
| 343 | 12.01 | 3.16 | 0.774 | 13.0 | 3.92 | 0.674 | 14.0 | 3.04 | 0.581 | 19.2 | 2.81 | 0.555 |
| 363 | 34.66 | 2.18 | 0.655 | 36.1 | 2.40 | 0.602 | 38.4 | 2.64 | 0.551 | 39.6 | 2.53 | 0.529 |
| 380 | 45.89 | 0.189 | 0.456 | 51.4 | .016 | 0.429 | 47.5 | 0.002 | o.390 | 52.87 | .00013 | 0.34 |
| 410 | 90.72 | 0.003 | 0.290 | 78.6 | 0.002 | 0.138 | 88.34 | 0.001 | 0.108 | 92.09 | 0.0005 | 0.0163 |

Table(2): The obtained values of the density of states $N(E_F)$,hopping distance(d ) and hopping energy W(eV)at different temperatures and thicknesses of $Ge_{10}Se_5Sb_{85}$

| | t=0.064cm | | | t=0.108 cm | | | t=0.138 cm | | | t=0.169 cm | | |
|---|---|---|---|---|---|---|---|---|---|---|---|---|
| Temperature (K) | $N(E_F)$ ($10^{15}$ $eV^{-1}$ $cm^{-3}$) | d ($10^{-6}$ m) | W(eV) | $N(E_F)$ ($10^{16}$ $eV^{-1}$ $cm^{-3}$) | d ($10^{-6}$cm) | W(eV) | $N(E_F)$ ($10^{16}$ $eV^{-1}$ $cm^{-3}$) | d ($10^{-6}$ cm) | W(eV) | $N(E_F)$ ($10^{16}$ $eV^{-1}$ $cm^{-3}$) | d ($10^{-6}$ cm) | W(eV) |
| 303 | 0.78 | 6.46 | 1.126 | 4.2 | 4.23 | 0.737 | 10.9 | 3.34 | 0.582 | 14.5 | 3.11 | 0.543 |
| 323 | 2.99 | 4.55 | 0.845 | 8.5 | 4.10 | 0.762 | 11.7 | 3.23 | 0.601 | 16.2 | 2.98 | 0.554 |
| 343 | 12.01 | 3.16 | 0.774 | 13.0 | 3.92 | 0.674 | 14.0 | 3.04 | 0.581 | 19.2 | 2.81 | 0.555 |
| 363 | 34.66 | 2.18 | 0.655 | 36.1 | 2.40 | 0.602 | 38.4 | 2.64 | 0.551 | 39.6 | 2.53 | 0.529 |
| 380 | 45.89 | 0.189 | 0.456 | 51.4 | .016 | 0.429 | 47.5 | 0.002 | o.390 | 52.87 | .00013 | 0.34 |
| 410 | 90.72 | 0.003 | 0.290 | 78.6 | 0.002 | 0.138 | 88.34 | 0.001 | 0.108 | 92.09 | 0.0005 | 0.0163 |

The region o-a is followed by a second one (a-b), which exhibits exponential behavior verifying the relation [31-33]:

$$I= I_o \exp( V/V_o)^{1/2} \quad (2)$$

where $I_o$ is the potential difference across the sample, $V_o = 4k_B^2T^2t/\beta_{PF}$, with $k_B$ being the Boltzmann constant, T is the ambient temperature of the sample, t is the sample thickness, and $\beta_{PF}$ is the Poole-Frenkel coefficient. The relationship between ln I and $V^{1/2}$ at different constant ambient temperatures for the sample t = 0.064 cm is shown in Figs.2a-2b, where $\beta_{PF}$ is determined and given in table 1. From this table it can be observed that $\beta_{PF}$ tends to decrease as the ambient temperature increases, while it exhibits increasing behavior as the sample thickness increases which indicates that the conduction mechanism in the (a-b) region of the OFF state follows either the Schottky emission [34] or the Poole-Frenkel-type conduction [35]. The region (b-c) in the OFF state seems to be linear as shown in Figs.2(b) and 2(c).

The samples exhibit a sudden change from a high-resistance (OFF) state to a negative-differential-resistance state (NDRS). The point at which the curves switch from the OFF state to the NDRS is called the turn-over point (TOP). The switching behavior is accompanied by the burning or heating of the conduction path which in turn may lead to the Joule heating effect during the initial stage of switching because of the high resistance of the samples that leads to an increase in the conduction path temperature ($T^\backslash$). This temperature was calculated for different thicknesses of the samples at constant ambient temperatures according to the relation [36,37]:

$$T^{\backslash}=T+\Delta T_J \quad (3)$$

where T is the ambient temperature and $\Delta T_J$ is the increase in the temperature of the conduction path, which is given by:

$$\Delta T_J = kT^2/[\Delta E_\sigma - kT] \quad (4)$$

where $\Delta E_\sigma$ is the activation energy of conduction and k is the Boltzmann constant. The calculated values of $T^{\backslash}$ and $\Delta T_J$ are given in Table 1, where it can be observed that as the ambient temperature increases, the temperature of the conduction path $T^{\backslash}$ increases consequently, $\Delta T_J$ increases, which enhances the proposed concept of the Joule heating effect and is in agreement with previously reported results [37-40]. The parameters related to the TOP, such as the threshold voltage $V_{th}$, threshold current $I_{th}$, threshold resistance $R_{th}$ and threshold power $P_{th}$, are calculated and their dependences on the sample thickness and temperature are discussed below.

### 3.2. Temperature dependence of the threshold voltage of $Ge_{10}Se_5Sb_{85}$

The temperature dependence of the threshold voltage ($V_{th}$) at different thicknesses for the sample $Ge_{10}Se_5Sb_{85}$ is shown in Fig.4 where an increase in $V_{th}$ as the ambient temperature increases is observed, verifying the relation [38]:

$$V_{th}=V_o \exp(\Delta E_v/ kT), \quad (5)$$

where $V_o$ is a temperature-independent parameter and $\Delta E_v$ is the threshold voltage activation energy related to the temperature of the conduction path. The linear plots between ln ($V_{th}$) and (1/T) can be understood [37,39] in terms of the electrothermal model for the pre-switching region as follows: The temperature dependence of the threshold voltage is an important factor that characterizes the robustness of the material against thermal degradation and hence the stability of the material for device applications [41]. The memory switching in chalcogenide glasses involves the formation of a conducting crystalline filament in the material, and hence a decrease in threshold voltage is expected [42]. Most amorphous materials contain dipoles dispersed randomly through the amorphous matrix. As an electric field is applied, these dipoles tend to orient in the direction of this field. The orientation process depends on the viscosity of the amorphous matrix as well as on the applied electric field. As the temperature of the conduction path increases, its viscosity decreases, enhancing the orientation process, up to the TOP. At this point, the resultant force of the resistance for dipole orientation in a viscous amorphous medium diminishes therefore, the switching process take occurs. Thus, as the ambient temperature increases, the viscosity of the conduction path decreases, therefore the field's ability to cause a maximum dipole orientation should decrease [37,39].

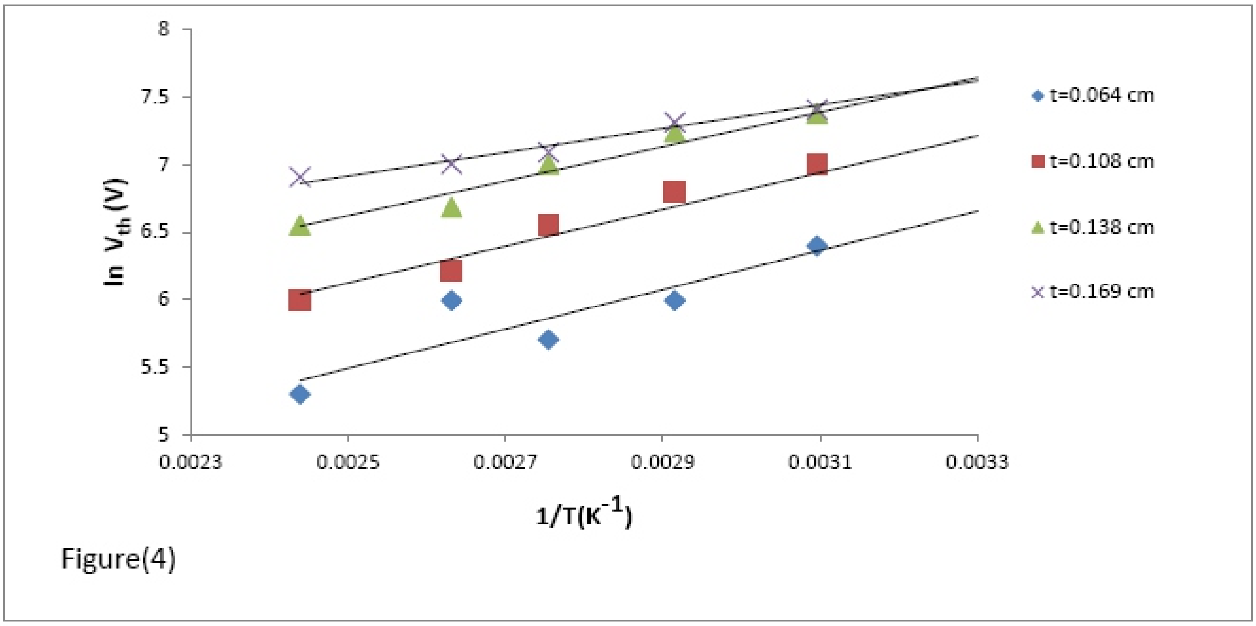


FIG. 4. The temperature dependence of the threshold voltage at constant thickness of the sample.

The thickness dependence of the threshold voltage for the investigated sample can be observed in Fig.4, where an increase in $V_{th}$ with the sample thickness is obtained. It has been suggested earlier [43] that $V_{th}$ varies with t, $t^{1/2}$, or $t^2$ depending on whether the mechanism responsible for switching is electronic, purely thermal, or electrothermal respectively. The results indicate the presence of electrothermal processes operating during the progress of the crystallization mechanism in the conduction path. It has been considered that as the sample thickness increases, the dissipated power inside the conduction path increases, which leads to an increase in the required field, consequently the threshold voltage increases, which is in agreement with previously reported results [44-46]. The values of $\Delta E_V$ at different thicknesses were deduced using the least-squares fitting method and are given in Fig.9. From this figure it can be observed that $\Delta E_V$ decreases as the thickness increases. The decrease in $\Delta E_V$ may be interpreted in terms of the localized state concept, which is calculated according to the relation [47]:

$$\beta_{PF} = \left[\frac{64\alpha^4\ 4}{(\ )}\right]^{1/4} \qquad (6)$$

where $\alpha^{-1}$ is the radius of the electron wave function, t is the sample thickness, and $N(E_F)$ is the density of localized states at the Fermi level. The calculated values of $N(E_F)$ are given in Table 2, where it can be observed that $N(E_F)$ tends to increase as the sample thickness increases, which results in a decrease in the hopping distance of the charge carriers between the filled and empty states. The calculated values of the hopping distance (d), according to the relation [48-50]:

$d = [9/(8 N(E_F) \pi \alpha k T)]^{1/4}$, are given in Table 2 where it can be noted that a decrease in d consequently results in a decrease in the required average hopping energy W(eV) between the filled and empty states. The calculated values of W(eV) according to the relation [50] : $W(eV) = [3/(4\pi d^3 N(E_F))]$ are given in Table 2.

### 3.3. Temperature dependence of the threshold current of $Ge_{10}Se_5Sb_{85}$

Fig.5 shows the temperature dependence of the threshold current $I_{th}$ for the investigated sample, which yields straight lines obeying the equation [38]:

$$I_{th} = I_o \exp(-\Delta E_i / kT), \quad (7)$$

where $I_o$ is an independent term and $\Delta E_i$ is the activation energy term related to the conduction mechanism. From this figure, it can be noticed that as the ambient temperature increases the threshold current increases, which may be attributed to an increase in the area of the conduction path where the crystallization process is enhanced. The deduced values of $\Delta E_i$ at different thicknesses are given in Fig.9. It can be observed that as the sample thickness increases, $\Delta E_i$ tends to decrease. The decreasing behavior may be attributed to the increased area of the conduction path.

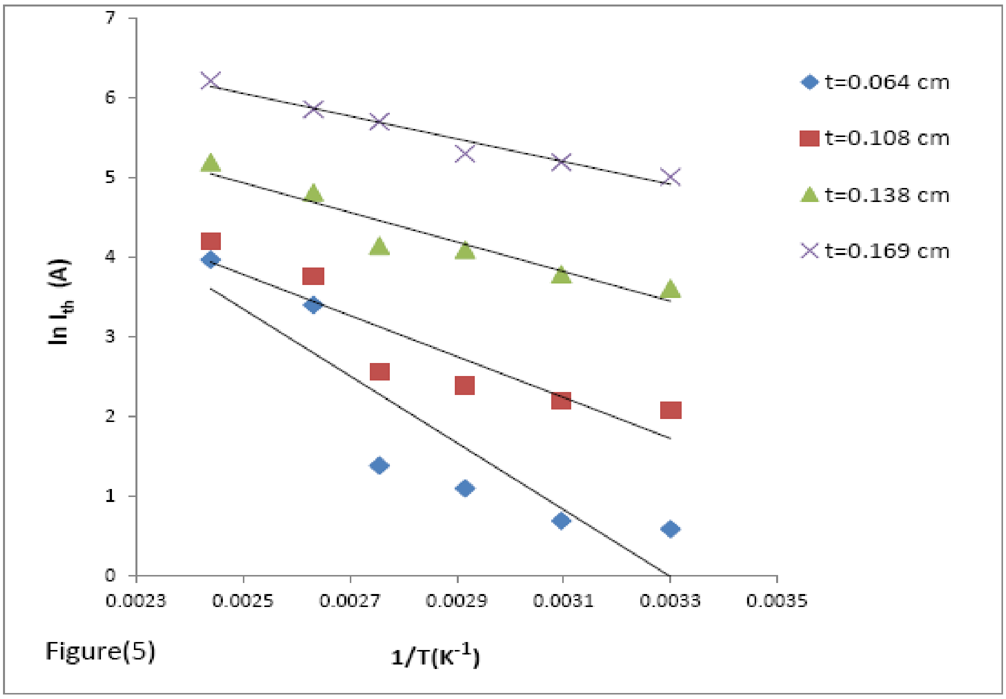


FIG. 5. The temperature dependence of the threshold current at constant thickness of the sample.

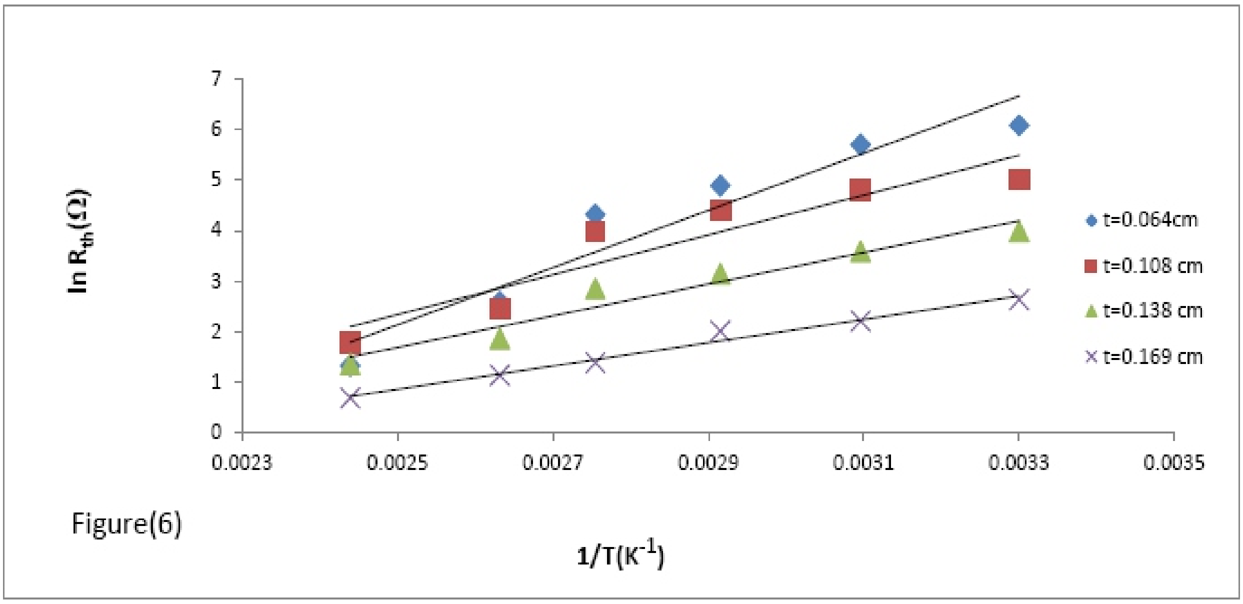


FIG. 6. The temperature dependence of the threshold resistance at constant thickness of the sample.

3.4. Temperature dependence of the threshold resistance of $Ge_{10}$ $Se_5$ $Sb_{85}$

Fig. 6 shows the temperature dependence of the threshold resistance $R_{th}$ for the investigated sample, which yields straight lines obeying the equation[38]:

$$R_{th}=R_o \exp(\Delta E_r /kT), \quad (8)$$

where $R_o$ is an independent term and $\Delta E_r$ is the activation energy term related to the conduction mechanism. It is observed that as the ambient temperature increases, the threshold resistance decreases. The threshold resistance increase as as the thickness of the sample increases. This may be attributed to an increase in the conduction path area. The values of $\Delta E_r$ were deduced for different thicknesses of the investigated sample using the least- squares fitting method and are given in Fig.9. From this figure it can be observed that $\Delta E_r$ tends to decreases gradually with the sample thickness, which is in agreement with previously reported results[37-46].

3.5. Temperature dependence of the threshold dissipated power of $Ge_{10}$ $Se_5$ $Sb_{85}$

The threshold dissipated power $P_{th}$ ($P_{th}=V_{th}\ I_{th}$) in the conduction path of the sample at the threshold voltage was calculated at different thicknesses of the investigated sample and is plotted (as shown in Fig.7 as ln $P_{th}$ against 1/T according to the relation[38]:

$$P_{th}=P_o \exp(-\Delta E_p /kT) \quad (9)$$

where $\Delta E_p$ is the activation energy at the threshold power. From Fig.7 it can be observed that $P_{th}$ decreases as the temperature increases. This may be due to the decrease in the number of collisions between the charge carriers in the samples. The values of $\Delta E_p$ were deduced and plotted as given in Fig.9 at different thicknesses of the investigated samples. It can be observed that $\Delta E_p$ decreases as the sample thickness increases which may be attributed to the deterioration of the scattering process between the charge carriers as a result of the enhanced process in the crystallization mechanism at the threshold point.

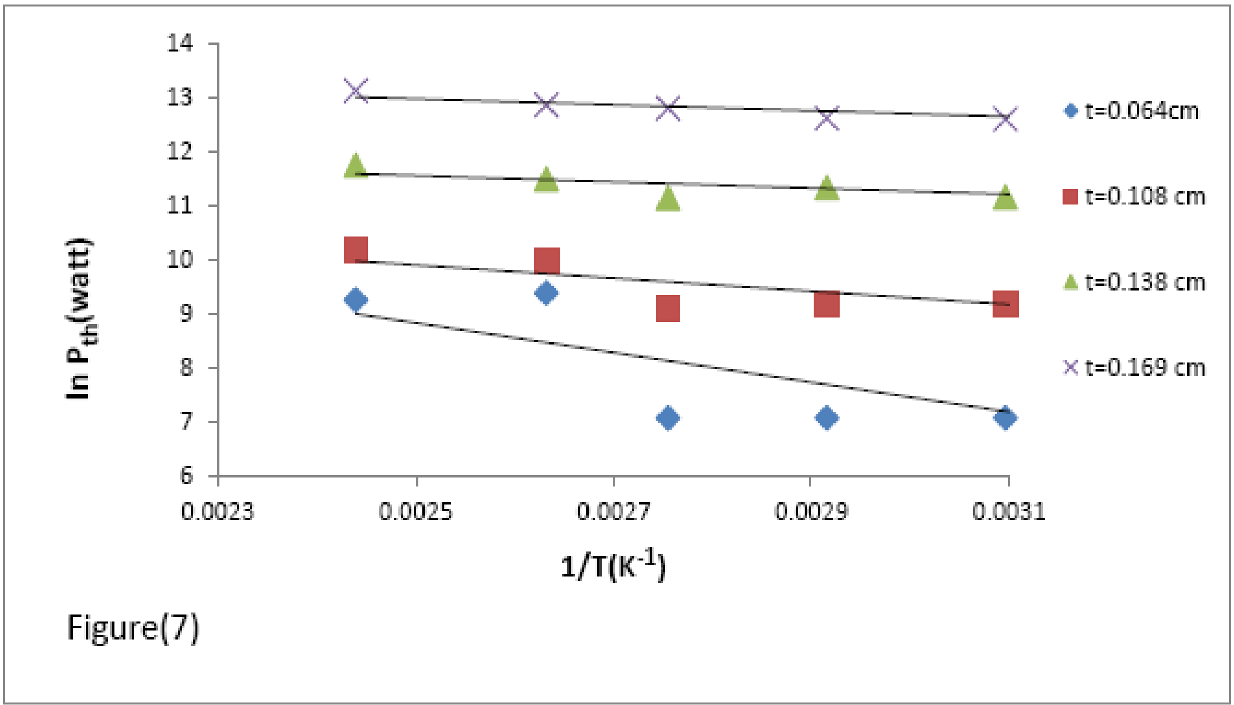


FIG. 7. The temperature dependence of the threshold power at constant thickness of the sample.

3.6. Temperature dependence of the threshold Electric field of $Ge_{10}\ Se_5\ Sb_{85}$

The threshold Electric field $E_{th}$ ($V_{th}$=t ) in the conduction path of the sample at the (TOP) was calculated at different thicknesses of the investigated sample and is plotted (as shown in Fig.8) as ln $E_{th}$ against 1/T obeying the relation,

$$E_{th}=E_o \exp (\Delta E_f /kT) \quad (10)$$

where $\Delta E_f$ is the activation energy at the (TOP). From Fig.8 it can be noticed that as the temperature of the sample increases ,the threshold electric field decrease .The deduced values of $\Delta E_f$ are plotted against the sample thickness as given in Fig.9. It can be noticed that as the sample thickness increases, $\Delta E_f$ decrease which may be attributed to the increasing in the orientation process of the dipoles in the direction of the applied electric field.

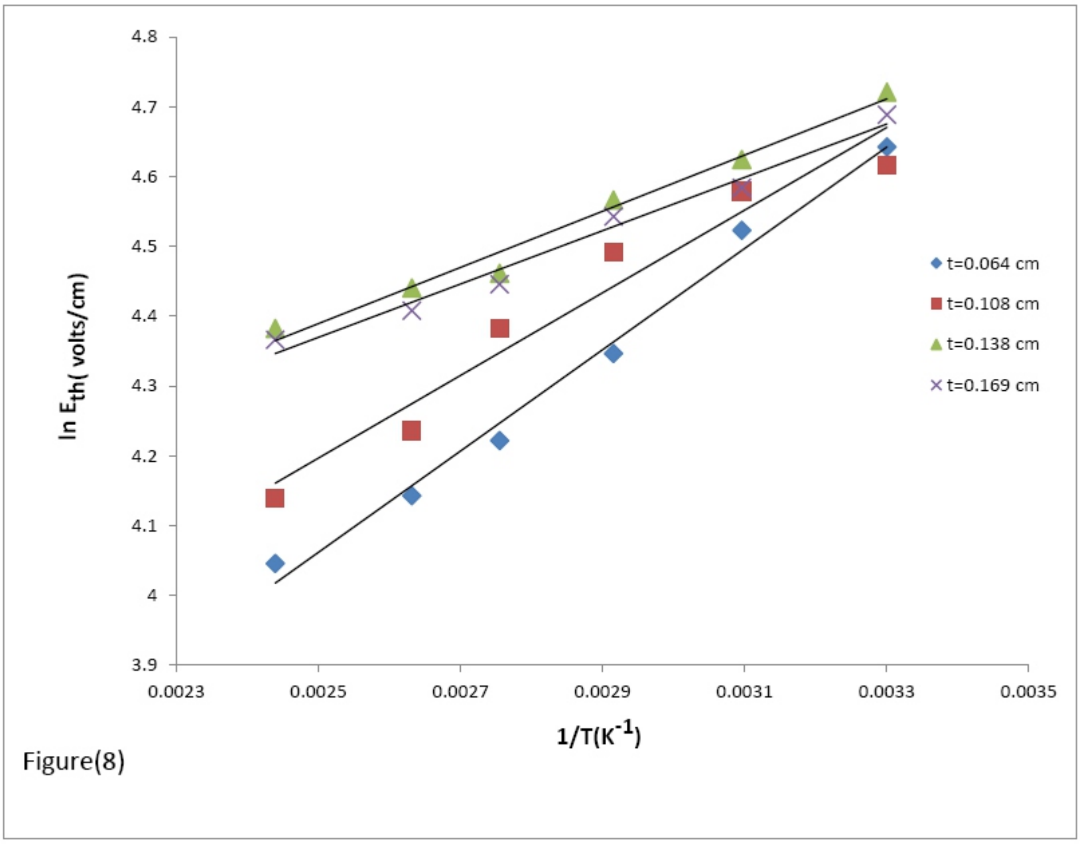


FIG. 8. The Temperature dependence of the threshold Electric field ($E_{th}$) of $Ge_{10}Se_5 Sb_{85}$

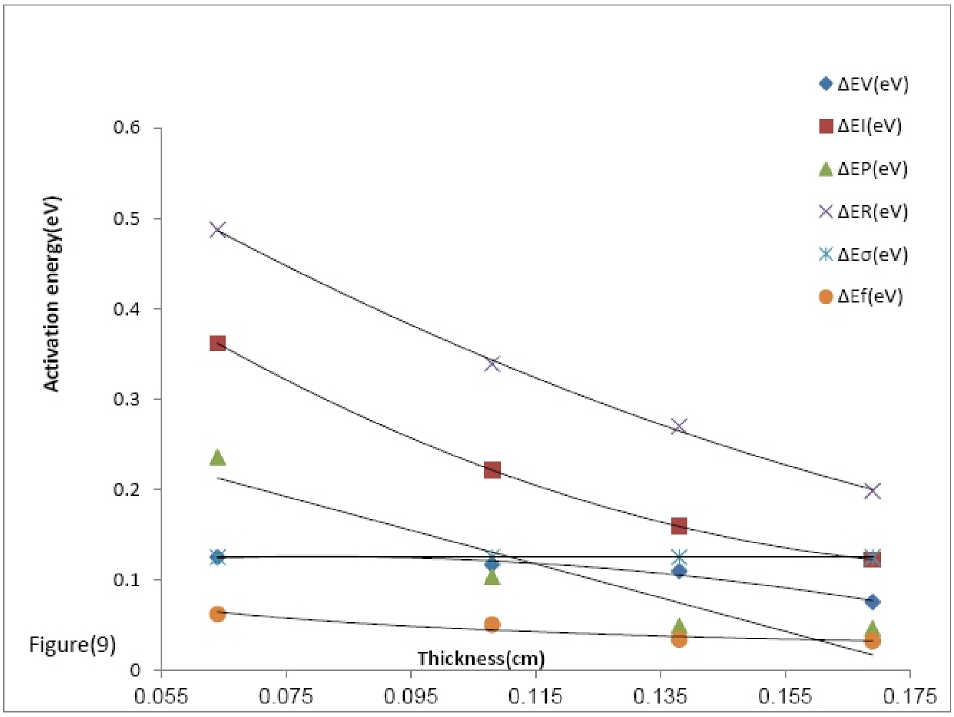


FIG. 9. The thickness dependence of the activation energy of $Ge_{10}Se_5 Sb_{85}$

## 4. CONCLUSION

Bulk chalcogenide glasses of $Ge_{10}Se_5Sb_{85}$ were prepared using the conventional melt quenching technique. The glassy nature of the prepared samples was confirmed by the X-ray diffraction technique. Switching phenomenon at the turn-over point (TOP) from a high-resistance state (OFF state) to a negative-differential resistance-state (NDRS) was detected where the threshold parameters such as threshold dissipated power ($P_{th}$) ,threshold voltage($V_{th}$),threshold current ($I_{th}$),threshold electric field ($E_{th}$) and threshold resistance ($R_{th}$)were determined at different thicknesses and ambient temperatures of the investigated samples. The activation energies of the investigated samples ($\Delta E_p$, $\Delta E_v$, $\Delta E_i$ ,$\Delta E_r$ and $\Delta E_f$) ,at the turn-over point,indicate a decreasing behavior with the sample thickness. The obtained values of the rise in the ambient temperature of the material($\Delta T_J$), temperature of the conduction path($T^{\backslash}$) and the Poole - Frenkel coefficient($\beta_{PF}$) at different temperatures and thicknesses were explained in terms of Poole-Frenkel effect.

## ACKNOWLEDGMENT

I'm gratefully acknowledge the deanship of scientific research, Jazan University, KSA, for the financial support, through the project number 7013/6/36.

## REFERENCES

[1] K. Tanaka,Y.os aka, M.Sugi, S.Lizima, M.Kikuchi: J.Non-Cryst.Sol.12 100 (1973)

[2] E. R. Shaabam: Physica B 373 211 (2006)

[3] Y. Sugiyama, R. Chiba, S. Fugimori and N. Funakoski: J.Non - Cryst. Sol. 83 (1990)

[4] S. R. Ovshinsky and H. Frizsche: Met.Trans.2 641 (1971).

[5] D. Adler: Sci.Am.236 36 (1977)

[6] E. A. Davis and N. F. Mott: Electronic Processes in Non-Crystalline Materials, Clarendon, Oxford, 1979

[7] D. Sarkar, G. Sanjeev and M.G.Mahesha,Appl.phys.A,119 49 (2015)

[8] R. Karuppaprnao,V. Ganesan and S. Asokan,Int. J. applied glass s cience 2(1) 52 (2011)

[9] G.Sreevidya V. ,D.V .S.Muthu,A.K.Sood and S.Asokan J.of Applied Physics. 115 164505 (2014)

[10] M.Malligavathy ,R.T.Ananth Kumar,Chandasree Das, S.Asokan, and D.Pathinettam Padiyan(J.non-Cryst.Solids 429 93 (2015)

[11] Chandasree Das, G.Mohan Rao and S.Asokan ,Materials Research Bulletin 49 388 (2014)

[12] V. Kumari,A. Kaswan, D. Patidar, N. S. Saxena and K. Sharma,Proceeding and Application of Cermaics 9(1) 61 (2015)

[13] 10th International conference on development and application systems, Suceava Romania,May 27-29(2010)

[14] N. S. Platakis: J. Non-cryst.Solids 27 331 (1978)

[15] A.M.Mio,S.Privitera,G.DArrigo,M.Ceppattelli,F.Gorelli,M.Santoro,M.Miritello ,R.Bini and E.Rimini J.Applied physics 18 064503 (2015)

[16] S. R. Ovshinsky: Phys. Rev.Lett.21 1450 (1968)

[17] A. S. Soltan and A. H. Moharram: Physica B 349 92 (2004)

[18] P. Pattanayak and S. Asokan: Solid State communications 142 698 (2007)

[19] J. A. Savage: J. Mater.Sci.7 64 (1972)

[20] J. Cornet: Ann.Chem.10 (1975) 239.

[21] C. Moss and J. P. Deneufville: Mater.Res.Bull.79 423 (1972)

[22] A. E. Owen and J. M. Robertson: IEEE Trans. Electron Dev. 20 105 (1973)

[23] N. Klein: Thin Solid Films 7 149 (1971)

[24] A.Adler, M.S.Shur, M.Silver and S.R.Ovshinsky:J.Appl.Phys.Lett.22 114 (1973)

[25] T. Kaplan and D.Adler: J Appl. Phys. Lett.19 418 (1971)

[26] D. M. Kroll: Phys. Rev. B 9 1669 (1974).

[27] B.J.Madhu.H.S.Jayanna,S.Asokan,J.Non-Cryst.Solids 355 459 (2009)

[28] A.Alegria, A.Arrubarrena, F.Sanz, J.Non-Cryst.Solids 58 17 (1983)

[29] G.C.Vezzoli, P.J.Walsh, L.W.Doremus, J.Non-Cryst.Solids,18 333 (1975)

[30] J.T.Devaraju, B.H.Sharmila, S.Aokan, K.V.Acharya, Philos.Mag.B 81 583 (2001)

[31] M.Burgelman,Solid State Electronics 20 523 (1977)

[32] G.A.Denton,G.M.Friedman,Schetzina,J.Appl.Phys.46 3004 (1957)

[33] M.M.Abdel-Aziz, Appl.Surf.Sci.253 2059 (2006)

[34] A.K.Jonsher, Thin Solid Films 1 213 (1967)

[35] J.J.O. Dwyer, The theory of Electrical Conduction and Breakdown in Solid Dielectrics, Clarendon Press, Oxford, 1979, P.220.

[36] S.Abouelhassan M.Sc. Thesis, Benha Uni.,Faclty of science (1987).

[37] M.K.El-Mansy, M.M.Elzaidia, S.Abouelhassan, A.A.Ammar, Appl.Phys. Commun.13 187 (1994)

[38] K.Nakashima , K.Kao, J.Non-Cryst.Solids 33 189 (1979)

[39] S.Abouelhassan, H.Khoder, Phys.stat.sol.(a)186 401 (2001)

[40] D.Roy,G.Varma,S.Asokan and C.Das, Int.J.Chemicalm Molecular, Nuclear, Material and Metallurgical engineering 10(6) 604 (2016)

[41] S.R.Ovshinsky, H.Frizsche, IEEE Trans. Electron Dev.20(2) 91 (1973)

[42] R.Lokesh, N.K.Udyashankar, S.Asokan, J.Non-Cryst.Solids 356 321 (2010)

[43] G.Jones, R.A.Collins, Phys.stat.sol.(a) 53 339 (1979)

[44] E.Mansour, Y.M.Moustfa, G.M.El-Dmarawi, S.AbdEl-maqsoud, H.Doweidr, Physica B 305 242 (2001)

[45] M.Gouda,H.Khodair,M.G.El-shaarawy,Mat.chem. and phys.120 608 (2010)

[46] L.L.Hench, J.Non-Cryst.Solids,2 250 (2009)
[47] N.F.Mott, E.A.Davis, Electronic Processes in Non-Crystalline Materials, Clarendon, Oxford, 1971.
[48] N.F.Mott, Philos.Mag.19 835 (1969)
[49] S.R.Elliott, Physics of Amorphous Materials, Longman Inc. , New York 1984
[50] R.M.Hill, Philos.Mag.24 1307 (1971).

# Synthesis and Characterization of Methyl ammonium Lead Tri-Chloride: An active layer in Perovskite Solar Cell

KamalSolanki [1], ShilpaSharma [*], Pratibha Shrivastava [#]

[1]Assistant Professor, Rungta College of Engineering &Technology, Raipur, Chhattisgarh, India.

*Associate Professor, Rungta College of Engineering& Technology, Raipur, Chhattisgarh, India.

[#] Professor, Rungta College of Engineering& Technology, Raipur, Chhattisgarh, India.

*Corresponding Author: Dr. Shilpa Sharma, Associate Professor, Rungta College of Engineering& Technology, Raipur, Chhattisgarh,

**A B S T R A C T**

In this work, the preparation of $CH_3NH_3PbI_{3-x}Cl_x$ using Dimethylformamide as solvent by a Magnetic stirrer & hydrothermal method was done. The favorably smooth and dense surface morphology of the $CH_3NH_3PbI_{3-x}Cl_x$ layers are obtained & investigated in by UV- Visible spectroscopy. The results indicate that the $CH_3NH_3PbI_{3-x}Cl_x$ thin film possesses appropriate morphological, optical and electronic properties to be suitable for perovskite solar cell applications. The photovoltaic devices have been investigated and optimized in detail by tuning layer thickness, processing temperature and time, annealing conditions of interfacial layers.

Keywords: Perovskite Solar cell, Active layer, Magnetic stirrer, Hydrothermal synthesis

## 1. INTRODUCTION

A perovskite solar cell includes aperovskite structured compound, most commonly a hybrid organic-inorganiclead or tin halide-basedmaterial, as the light-harvesting active layer. Perovskite materials such as methyl ammonium are cheap to buy and simple to manufacture, the rapid improvement of perovskite solar cells has made them the rising star of the photovoltaic's world and of huge interest to the academic community. Since their operational methods are still relatively new, there is great opportunity for further research into the basic physics and chemistry around perovskites. Furthermore, as has been shown over the past two years the engineering improvements of perovskite formulations and fabrication routine to significant increases in power conversion efficiency.

The perovskite lattice arrangement is demonstrated below. As with many structures in crystallography, it can be represented in multiple ways. The simplest way to think about a perovskite is as a large atomic or molecular cation (positively-charged) of type A in the centre of a cube. The corners of the cube are then occupied by atoms B (also positively-charged cations) and the faces of the cube are occupied by a smaller atom X with negative charge (anion).

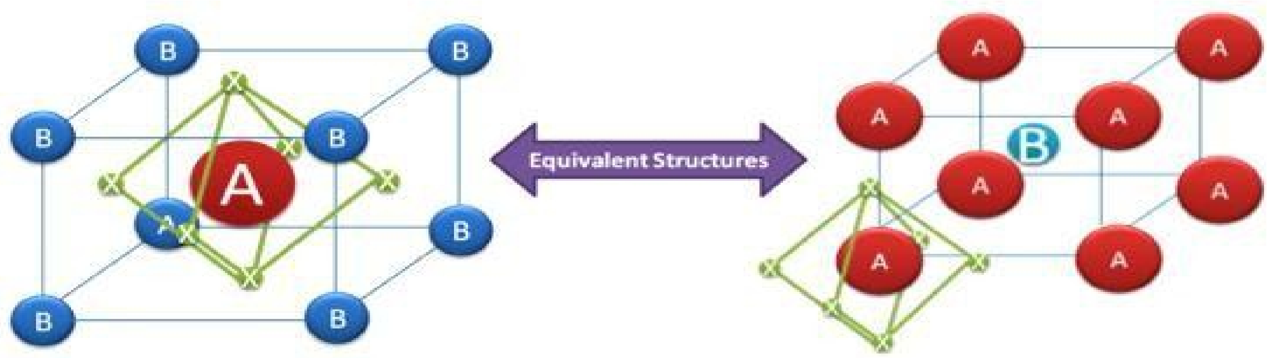


Figure no 1: Crystal structure of CH3NH3PbX3 Perovskite (X=I,Br, andCl).

In the case of perovskite solar cells, the most efficient devices so far have been produced with the following combination of materials in the usual perovskite form ABX3:

A=An organic cation-methylammonium$(CH_3NH_3)^+$

B =A big inorganiccation-usually lead (II) $(Pb^+)$

$X_3$=A slightly smaller halogenanion– usually chloride $(Cl^-)$ or iodide$(I^-)$

Since this is a relatively general structure, these perovskite-based devices can also be given a number of different names, which can either refer to a more general class of materials or a specific combination. As an example of this, we've created the below table to highlight how many names can be formed from one basic structure.

| A | B | X |
|---|---|---|
| ORGANO | METAL | TRI-HALIDE |
| METHYL AMMONIUM | LEAD | TRI IODIDE |
| | PLUMBATE | TRI-CHLORIDE |

3. RESULT & DISCUSSION:

3.1 Optical property of Perovskite solution

The UV-VISIBLE measurement was carried on the Perovskite solution ($CH_3NH_3PbI_{3-x}Cl_x$), results by both the method were concluded, in case of magnetic stirrer method it was founthat the λ $_{max}$ is 390nm, and in case of Hydrothermal synthesis, found the diffraction peak at 380nm and 420nm, which indicates different shape & size of material (morphology difference) which is relatively good for Perovskite solar cell.

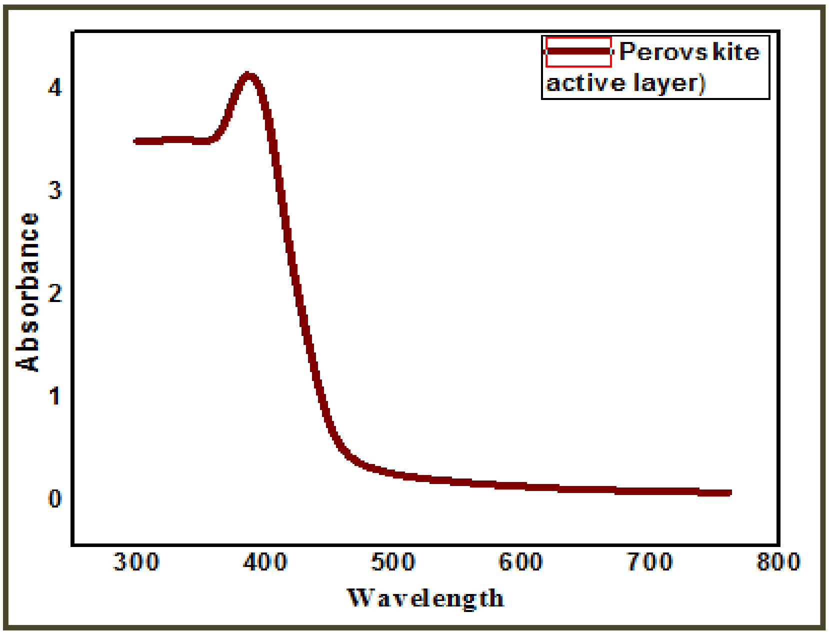


Figure 2: Absorption spectra of Active layer via Magnetic stirrer.

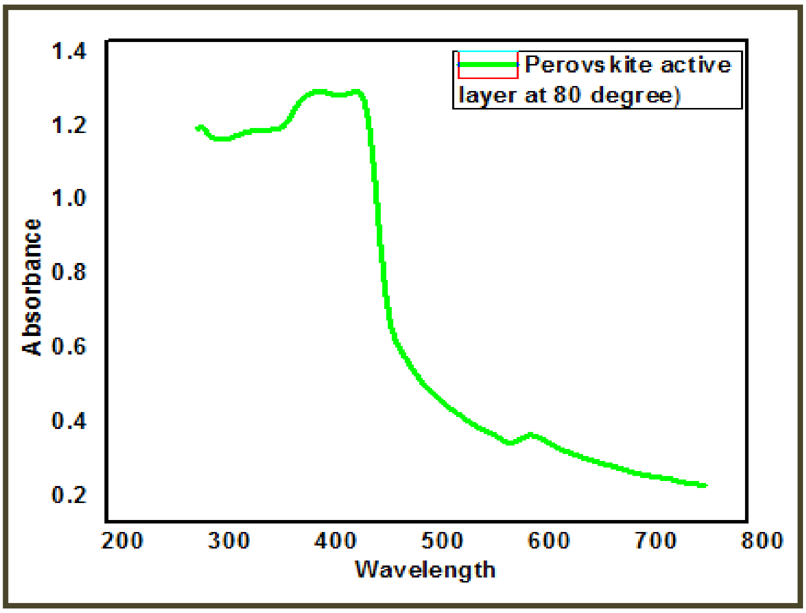


Figure 3: Absorption spectra of Active layer via Hydrothermal treatment.

3.2 Energy Dispersive X-ray spectroscopy:

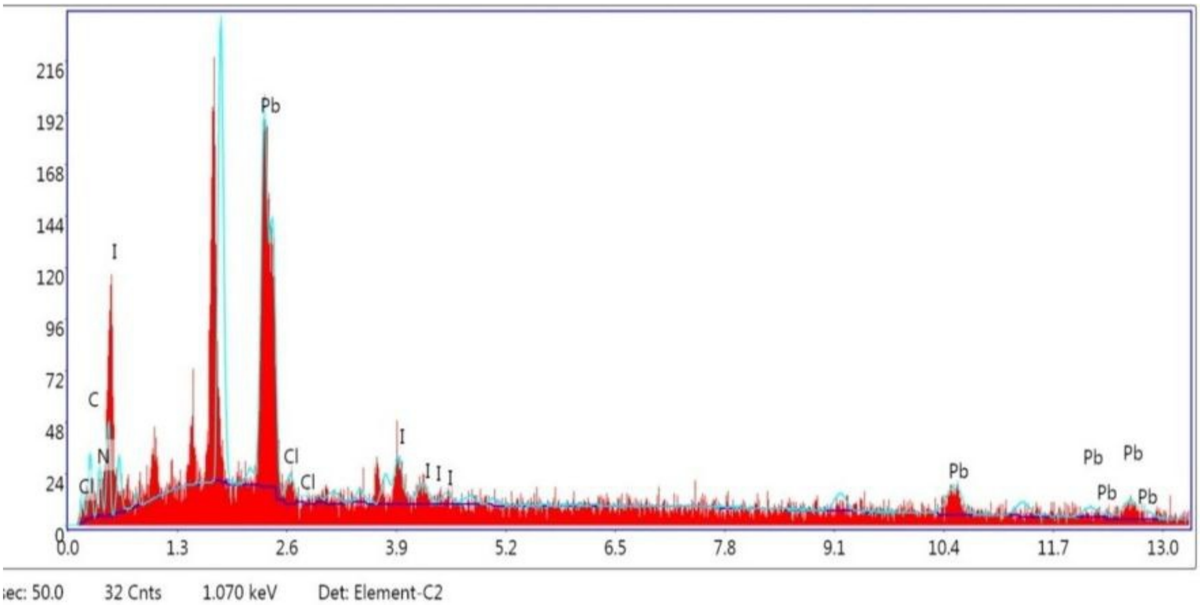


| ELEMENT | WT.% | ATOMIC WEIGHT% |
|---|---|---|
| CK | 5.83 | 31.50 |
| NK | 8.36 | 38.71 |
| PbM | 71.28 | 22.32 |
| ClK | 0.02 | 0.04 |
| IL | 14.51 | 7.42 |

Figure. 4 : EDX graph representing the various compounds present in the perovskite Solution with weight percentage also shown in figure.

3.3 Dual thermal annealing engineering technique

Fabrication of most-promising $CH_3NH_3PbI_{3-x}Cl_x$ based perovskite solar cell in ambient condition is excessively essential to industrialize this revolutionary development. In this research work, an efficient, facile and economical technique has been developed to fabricate $CH_3NH_3PbI_{3-x}Cl_x$ perovskite solar cell in ambient condition which is termed as dual-step thermal engineering technique .In this dual-step thermal engineering technique, the perovskite precursor solution has been spin coated over a mildly hot substrate which was heated at 60°C for 10min followed by annealing at 80°C for 30 min immediately after spin Coating.

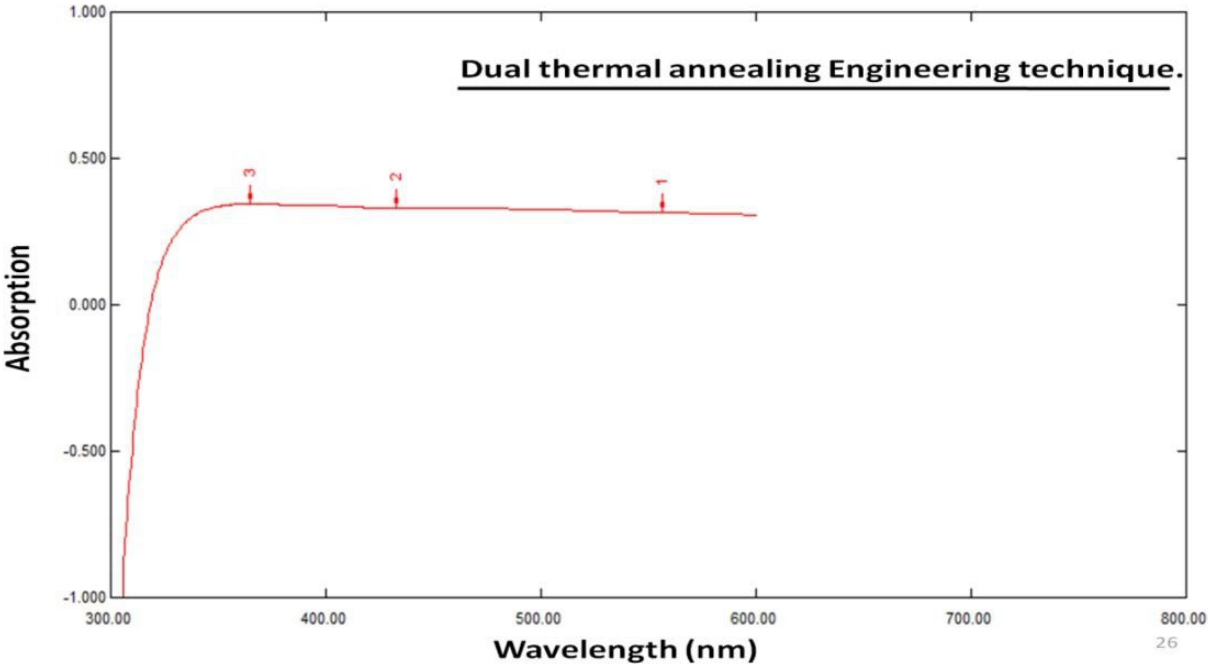


Figure 5: Absorption spectra of $CH_3NH_3PbI_{3-x}Cl_x$ Perovskite Film

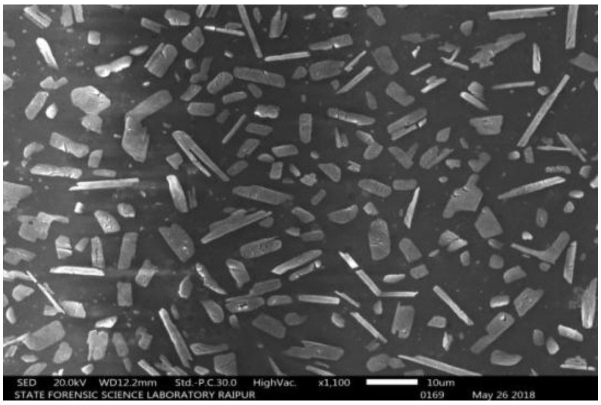


Figure 6: SEM morphology image of $CH_3NH_3PbI_{3-x}Cl_x$.

CONCLUSION

The Perovskite solution using Methyl ammonium iodide, Lead chloride & dimethyl formamide is synthesized by using magnetic stirrer & hydrothermal process. The characterization of the prepared perovskite solution was done from spectroscopic measurement. It is found that enhanced absorption Spectrum of $CH_3NH_3PbI_{3-x}Cl_x$ via hydrothermal synthesis are obtained at 80°C with good optical properties & it was also found that two diffraction peaks were obtained at 380 nm & 400 nm because of heating effects which indicates difference in morphology & its relatively good for Perovskite solar cell which will enhanced absorption spectra of Perovskie layer & it also enhance the power conversion efficiency of Perovskite solar cell. Overall, the simple & stable perovskite solution that is developed is a viable candidate of active layer in Perovksite solar cell.

## REFERENCES


[1] Moyez, Sk Abdul, and Subhasis Roy. "Dual-step thermal engineering technique: A new approach for fabrication of efficient CH 3 NH 3 PbI 3-based perovskite solar cell in openaircondition." *Solar Energy Materials and Solar Cells* 185 (2018): 145-152.

[2] Tonui, Patrick,etal."Perovskites photovoltaic solar cells:An overview of current status."

[3] *Renewable and Sustainable Energy Reviews* 91(2018):1025-1044.

[4] Chen, Yichuan, et al. "Large-area perovskite solar cells–review of recent progress andissues."*RSC Advances* 8.19 (2018): 10489-10508.6.

[5] Kangsabanik, Jiban, et al. "Double perovskites overtaking the single perovskites: A set of new solar harvesting materials with much higher stability and efficiency. "*Physical Review Materials* 2.5 (2018): 055401.

[6] Ibn-Mohammed, Taofeeq, et al. "Perovskite solar cells: An integrated hybrid life cycle assessment and review in comparison with other photovoltaic technologies." *Renewable and Sustainable Energy Reviews* 80 (2017): 1321-1344.

[7] Singh,Trilok,Jai Singh,and Tsutomu Miyasaka. "Role of Metal Oxide Electron-Transport Layer Modification on the Stability of High Performing Perovskite Solar Cells."*Chem Sus Chem* 9.18 (2016): 2559-2566.

[8] Li, Hangqian, etal." A modified sequential deposition method for fabrication of perovskite solar cells."*Solar Energy* 126 (2016):243-251.

[9] Manser, Joseph S.,JeffreyA.Christians,and PrashantV.Kamat."Intriguing optoelectronic properties of metal halide perovskites." *Chemical reviews* 116.21 (2016):12956-13008.

[10] D'Innocenzo,Valerio, et al."Excitons versus free charges in organo-lead tri-halide perovskites."*Naturecommunications* 5 (2014): 3586.

[11] Lee, Michael M.,etal."Efficient hybrid solar cells based onmeso-superstructured organo metalhalide perovskites." *Science* (2012): 1228604.

# CMOS Nonmagnetic Circulator and Band-Selection Balun-Low Noise Amplifier with RF Self-Interference Cancellation for Advanced In-Band Full-Duplex Transceiver

**Seokwon Lee, Yonghwan Lee, Chanhee Cho, and Kuduck Kwon**

## ABSTRACT

*In this paper, a CMOS nonmagnetic circulator and band-selection balun-low noiseamplifier (LNA) with RF time-domain selfinterference cancellation (SIC) are presented torealize an advanced In - band full-duplex (IBFD)transceiver. The capacitor (C)-inductor (L)-Cnonmagnetic circulator based on an N-path filter andtime-domain RF SIC with multi delay tap areemployed to achieve low receiver (RX) andtransmitter (TX) insertion losses and high SIC.Because the circulator does not possess out-of-band(OB) blocker rejection capability, the band-selectionN-path balun-LNA is proposed to replace thefunctionality of the OB blocker rejection of theconventional SAW filters. Simulated in a 65 nmCMOS process, the circulator and balun-LNA withRF canceller achieved a noise figure of 6.6 dB, voltagegain of 17 dB, and SIC of 58 dB. It has an active diearea of 1.61 mm2, and consumed 14 mA for a nominalsupply voltage of 1 V.*

***Index Terms—N-path filter, circulator, isolation, delay,low noise amplifier, low-loss, self-interference, selfinterference cancellation, out-of-blocker***

## 1. Introduction

Recently, in-band full-duplex (IBFD) wireless communication technology has garnered signiicant attention as a key technology for 6G and beyond 5G cellular applications [1, 2]. In particular, considering that 5G new radio (NR) networks will continue to operate alongside 6G, research on the IBFD technology, which can efficiently utilize the existing limited frequency resources, is crucial. Unlike the traditional half-duplex (HD) approach, which divides the transmission into separate time or frequency slots, the IBFD technology enables simultaneous uplink and downlink transmissions in the same time and frequency band, ideally doubling the frequency utilization efficiency and data rates compared with HD. Additionally, it can reduce the latency compared with time-division duplexing (TDD).

However, in IBFD transceivers, the output signal from a transmitter (TX) can cause a strong self-interference (SI) at the receiver (RX), degrading its signal-to

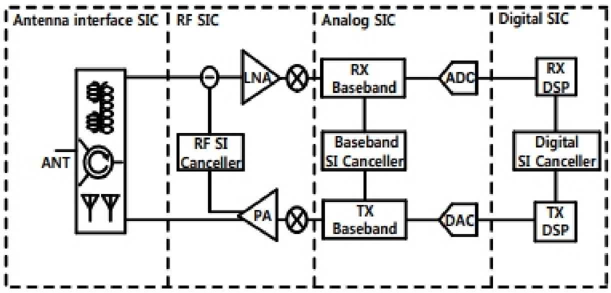


**Fig. 1.** Block diagram of the conventional IBFD transceiver.

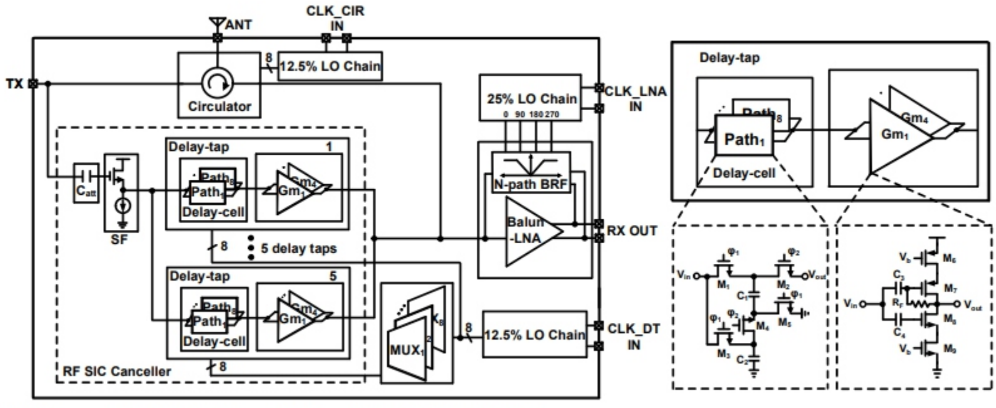


**Fig. 2.** Proposed CMOS circulator and band-selection LNA with RF SIC

noise/distortion ratio (SNDR). Therefore, achieving a sufficient self-interference cancellation (SIC) is essential for implementing IBFD transceivers. Fig. 1 shows a block diagram of a conventional IBFD transceiver. SIC techniques in IBFD transceivers can be categorized into antenna interface SIC [3-7], RF SIC [8-10], analog SIC [11, 12], and digital SIC [13], with active research ongoing in each domain. To prevent SNDR performance degradation caused by the strong SI signal on the RX side, it is crucial to achieve high SIC performance in the antenna interface and RF domains.

This alleviates the linearity requirements of the lownoise amplifier (LNA) and the following blocks. Representative antenna interface SIC techniques include an electrical-balanced duplexer (EBD) based on hybrid transformers and nonmagnetic circulators. While the EBD offers excellent TX-RX isolation of over 50 dB, it has the drawback of more than 3 dB insertion loss (IL) in both the TX and RX paths, impacting the power amplifier (PA) efficiency and RX noise figure (NF). On the other hand, nonmagnetic circulators exhibit TX and RX ILs of approximately 1-2 dB, but their TX-RX isolation is relatively poor at approximately 20-30 dB.

However, compared with the SAW/FBAR duplexers used in FDD systems, both EBD and nonmagnetic circulators lack a strong out-of-band (OB) blocker rejection capability at the antenna, making them unable to mitigate the SNR degradation caused by strong OB blockers. Conventional IBFD research primarily focuses on enhancing the SIC performance, neglecting the degradation of the RX SNDR due to strong OB blockers. For the successful commercialization of IBFD transceivers without using additional SAW filters at the RF front end, these aspects should also be carefully considered.

In this paper, a band-selection balun-LNA employing a feedback network of a differential-to-single-ended N path notch filter is presented to provide OB blocker rejection and enhance the blocker tolerance of the RX. A capacitor(C)-inductor (L)-C nonmagnetic circulator based on an N-path filter and a time-domain RF SIC with five delay taps is also introduced. This paper is structured as follows. Section II presents detailed circuit designs. Section III shows the simulation results. Finally, Section IV concludes the study.

## II. PROPOSED CMOS CIRCULATOR AND BAND-SELECTION LNA WITH RF SIC

Fig. 2 depicts the proposed CMOS circulator and band-selection LNA with RF SIC. The circulator performs the first SIC, where the time-domain RF SIC with delay taps performs the second SIC at the LNA input. This two-stage SIC process prevents saturation of the LNA and subsequent circuits owing to strong SI signals or degradation of the SNDR owing to the nonlinearity of the LNA and subsequent blocks. The band-selection balun-LNA that uses the D2S N-path notch filter feedback rejects the OB blocker and enhances the blocker tolerance of the RX.

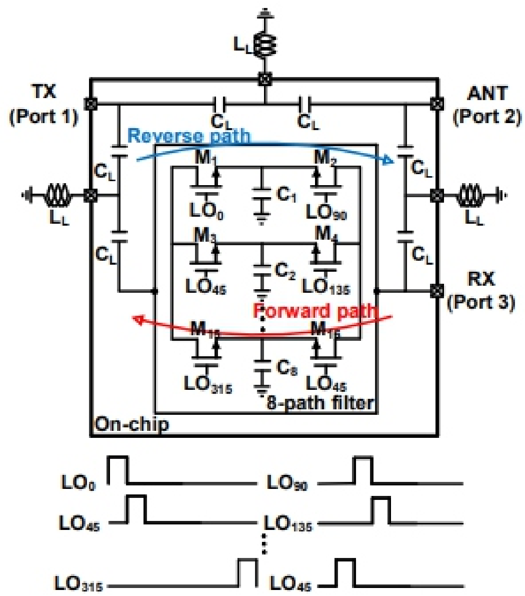


**Fig. 3.** Schematic of the C-L-C nonmagnetic circulator based on N-path filter

### A. C-L-C Nonmagnetic Circulator based on N-pathFilter

Fig. 3 shows a schematic of the circulator used for the antenna interface SIC. The circulator employs the topology of an integrated nonmagnetic N-path filter based C-L-C circulator [14]. In the 3-port circulator, each λ/4 transmission line is replaced by a lumped C-L-C section. External inductors are used to achieve a high Q factor. This structure enables CMOS integration and unidirectional propagation with minimal losses. Two-port N-path filters can introduce phase nonreciprocity by offsetting the timing of the two sets of switches. This leads to nonreciprocal phase responses (+90 o /-90 o in the forward and reverse directions) and enables the creation of a CMOS gyrator. Subsequently, a 3λ/4 transmission line can be wound around this gyrator to facilitate signal propagation in a single direction. By connecting the three ports on this transmission line with a spacing of λ/4, a three-port circulator can be realized [15].

Fig. 4 shows the simulated frequency response of the two-port N-path filter in two directions. Fig. 5 shows the simulated TX IL, RX IL, and TX-RX isolation (i.e., the antenna interface SIC). At 700 MHz, the TX IL and RX IL are 2.2 dB and 2.3 dB, respectively. The TX-RX isolation is greater than 37 dB for a channel bandwidth (CHBW) of 20 Mhz.

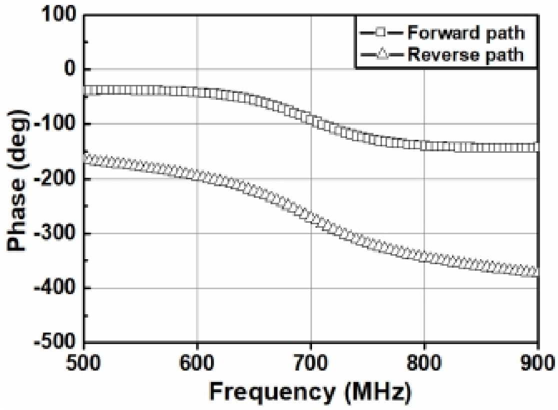


**Fig. 4.** Simulated phase response of the two-port *N*-path filter with two sets of switching time.

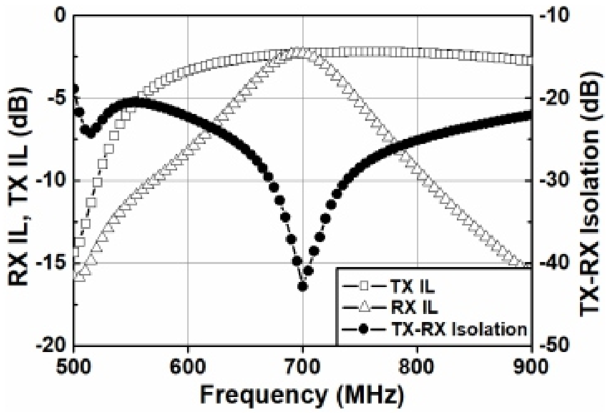


**Fig. 5.** Simulated TX IL, RX IL and TX-RX isolation.

**B. N-path Balun-LNA**

The proposed band-selection balun-LNA employs D2S N-path band rejection filter (BRF) feedback to eliminate OB blockers and improve blocker tolerance [16]. As shown in Fig. 6, it is based on a gain-boosted N-path filter LNA structure. It consists of two common-source (CS) amplifiers, a differential current balancer (DCB), and an LC tank. Two CS amplifiers (M1,2 ) perform single-to-differential conversion. The DCB comprises cascade transistors (M3,4 ) and cross-coupled capacitors (CC1,2 ). It makes the output currents become IOUTP = - IOUTN [16]. The voltage gain of the N-path balun-LNA from the voltage source VS with a source resistance RS to the output VOUT can be expressed as [16]

$$A_{V,NpathBalun} = \frac{V_{OUT}}{V_S} = \frac{(1-g_m Z_{FB}(s))Z_L(s)}{R_S(1+g_m Z_L(s)) + Z_{FB}(s) + Z_L(s)}. \quad (1)$$

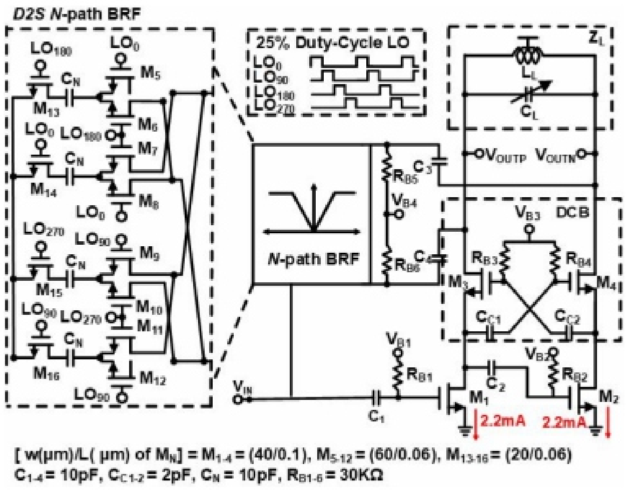


**Fig. 6.** *N*-path balun-LNA.

where ZFB(s) and ZL(s) are the impedances of the frequency-selective D2S N-path BRF feedback network and LC tank, respectively. The D2S N-path BRF feedback network can be simplified using an equivalent RLC model (RP, CP, and LP) as follows:

$$Z_{FB}(s) = R_{SW} + \frac{sL_P R_P}{s^2 L_P C_P R_P + sL_P + R_P} \quad (2)$$

$$R_P \approx \frac{N\sin^2(\pi/N)}{N((\pi/N)^2 - \sin^2(\pi/N))}(R_S + R_{SW} + \frac{Z_L}{2}) \quad (3)$$

$$C_P \approx \frac{\pi^2}{2N\sin^2(\pi/N)} C_N \quad (4)$$

$$L_P \approx \frac{1}{(2\pi f_{LO})^2 C_P} \quad (5)$$

where N is the number of paths, RSW is the switch resistance, and CN is the series capacitance.
Fig. 7 shows the simulated voltage gain of the N-path balun-LNA. It has a voltage gain of more than 20 dB in the low band of the 5G NR sub-6GHz. In addition, the LNA can reject OB blockers by more than 20 dB. Fig. 8 shows the simulated NF of the N-path balun-LNA. The NF is from 3.45 to 3.7 dB across in Band 71/n71, Band 28/n28, and Band 5/n5.

**C. RF SIC**

A block diagram of the RF SIC is shown in Fig. 2. The RF SIC consists of an attenuator with Catt
, a source follower, and five delay taps with a 12.5% duty-cycle LO chain. Catt attenuates the strong TX signal to prevent

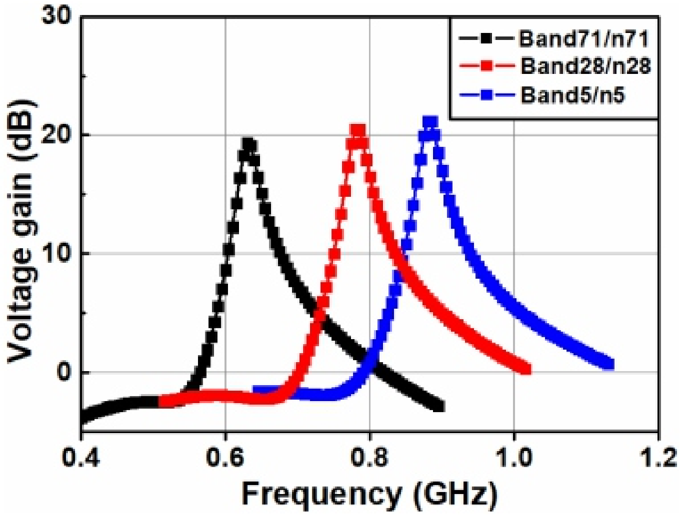


**Fig. 7.** Simulated voltage gain of the *N*-path balun-LNA.

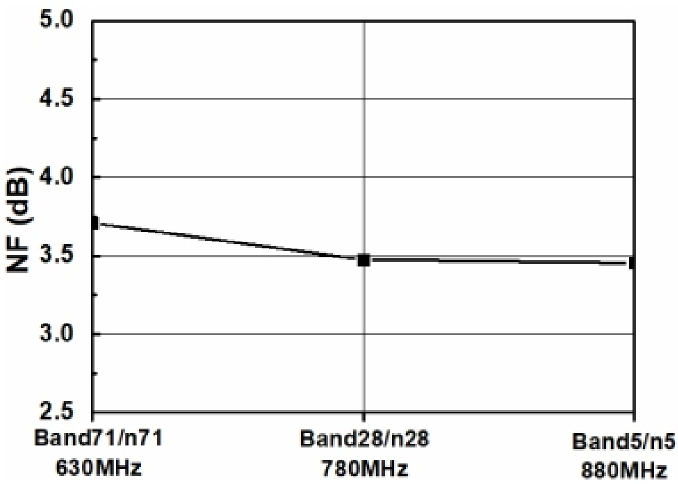


**Fig. 8.** Simulated NF of the *N*-path balun-LNA.

saturation of the RF SIC circuits. The amount of attenuation is determined by the ratio of Catt to Cgs of the source follower. Each delay tap can independently provide individual delays. Each delay tap consists of a delay cell and 2-bit controlled inverter-type gm cell. The delay cell comprises eight delay paths. The delay path employs a time-interleaved switched-capacitor topology, as shown in Fig. 2. This delay cell can provide seven distinct delay options ranging from 250 ps to 1.75 ns with a resolution of 250 ps [17]. Using four delay taps, different predefined values were used to implement distinct fixed group delay settings. The final delay tap was controlled using a multiplexer, providing flexibility in adjusting the group delay and allowing for seven different group delay settings with the use of five delay taps. Fig. 9 shows the simulated group delays. The proposed delay taps could control the group delay from 250 ps to 1.75 ns with a resolution of 250 ps

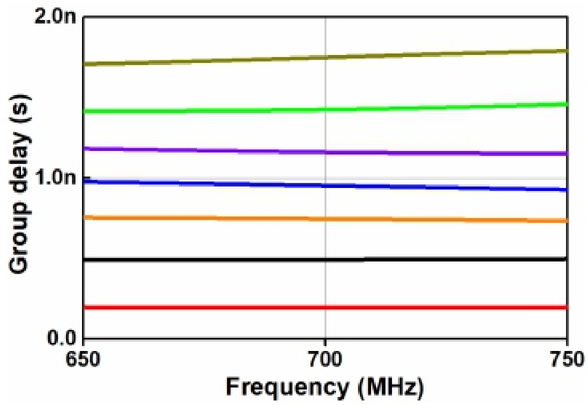


**Fig. 9.** Simulated group delays.

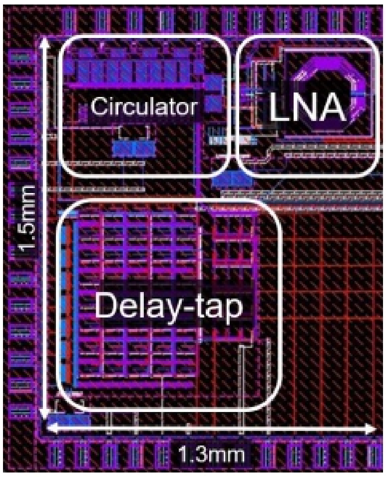


**Fig. 10.** Layout of the CMOS circulator and band-selection balun-LNA with RF SIC.

Furthermore, 2-bit controlled inverter-type gm cells were employed to adjust the magnitude of the RF SIC signal with the SI signal from the CMOS circulator.

**III. SIMULATION RESULTS**

The proposed C-L-C nonmagnetic circulator based on an N-path filter and time-domain RF SIC with five delay taps were designed using a 65 nm CMOS process. Fig. 10 illustrates the layout of the CMOS circulator and band-selection balun-LNA with RF SIC circuits. The active area without bond pads was 1.61 mm 2 . A DC bias current of 14 mA was applied at a supply voltage of 1 V. Fig. 11 shows the simulated S11 of the circulator. The S11 is less than -10 dB. Fig. 12 shows the simulated voltage gain from the antenna port to the LNA output of the circulator and N-path balun-LNA. This shows that the voltage gains from the antenna port to the LNA output

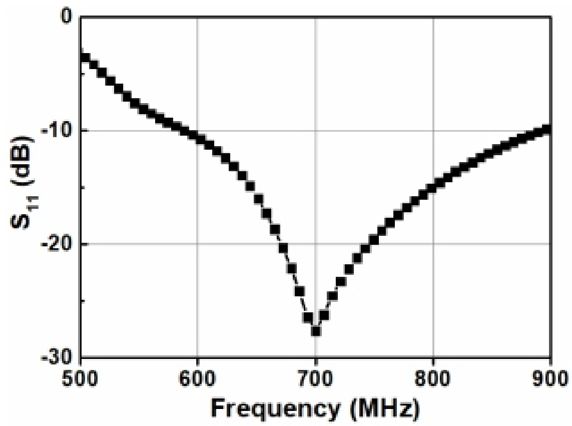


**Fig. 11.** Simulated $S_{11}$ of the circulator.

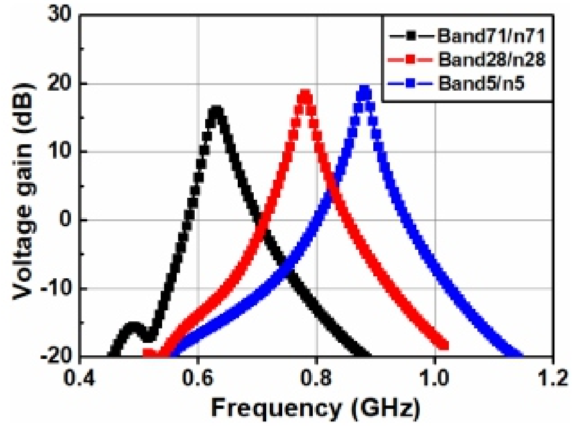


**Fig. 12.** Simulated voltage gain from antenna port to LNA output.

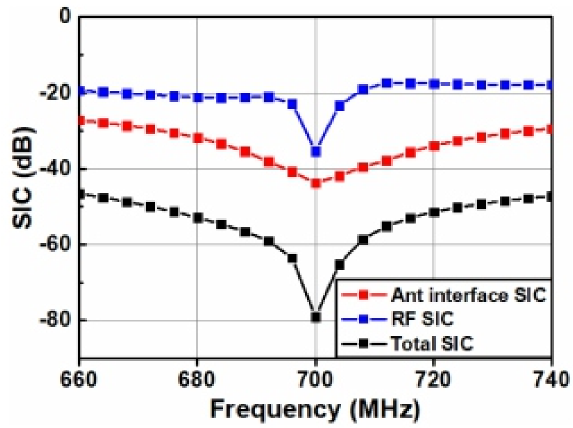


**Fig. 13.** Simulated SIC.

are greater than 17 dB in Band 71/n71, Band 28/n28, and Band 5/n5. The OB blocker rejection exceeded 30 dB at the frequency offset of 100 MHz. The simulated SIC performance are illustrated in Fig. 13. The simulated antenna interface SIC and RF SIC are greater than 38 dB and 20 dB at 700 MHz with the CHBW of 20 Mhz,

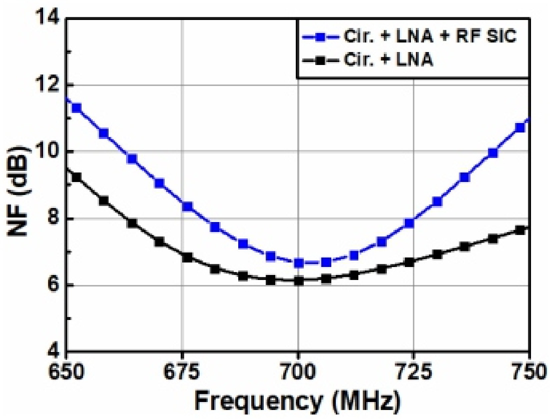


**Fig. 14. Simulated NF.**

respectively. The total SIC exceeded 58 dB for the CHBW of 20 MHz. Fig. 14 shows the simulated NF of the circulator and N-path balun-LNA with RF SIC. RF SIC circuits degrade the NF by 0.5 dB. The IIP3s of the circulator and N-path balun-LNA with RF SIC were also characterized in terms of the presence of in-band (IB) and OB blockers, as shown in Fig. 15 and 16. The twotone test conditions for the IB IIP3 were f1 = fLO + 1 Mhz, f2 = fLO + 1.1 MHz, and pf1 = pf2 = −44 dBm. The simulated IB IIP3 with the N-path bandpass filtering was -3.9 dBm to -3.6 dBm. The two-tone test conditions for the OB IIP3 were f1 = fLO + 40 MHz, f2 = fLO + 81 Mhz, pf1 = pf2 = −44 dBm. The simulated OB IIP3 with the Npath bandpass filtering was 4 dBm to 5 dBm. Compared to the configuration without the N-path filtering, there is around a 2 dB improvement in the IB IIP3 and a notable enhancement of 7-8 dB in the OB IIP3. Table 1 lists the performance summary of the proposed circulator and N path balun-LNA with RF SIC circuits and a comparison with previous state-of-the-art works. In this study, we implemented RF band selection capabilities in the LNA, taking into account the performance degradation caused by the OB blockers in the IBFD transceiver. Compared to other works, this work exhibits high RF SIC performance. However, it has relatively higher NF characteristics. For fair performance comparison, the following figure of merit (FOM) was used, which is the product of the SIC and fractional bandwidth [23]:

$$FOM = 10Log(SIC[\text{Mag}] \times \frac{CHBW[\text{MHz}]}{f_c[\text{MHz}]}), \quad (6)$$

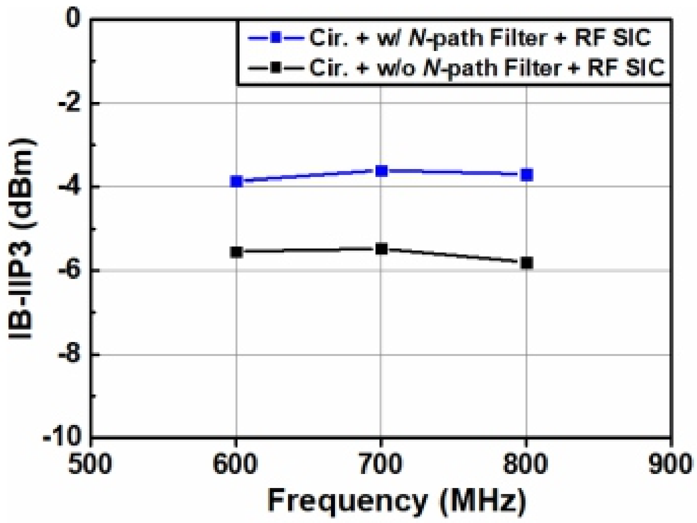


Fig. 15. Simulated IB-IIP3.

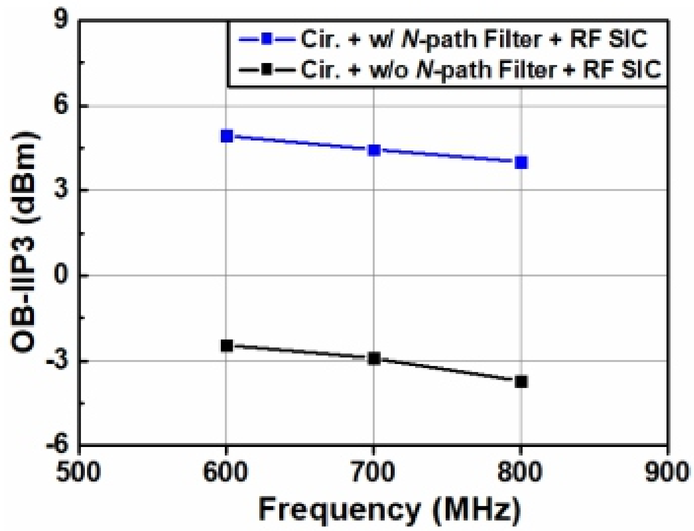


**Fig. 16. Simulated OB-IIP3.**

where fc is a center frequency. As shown in Table 1, the proposed work achieves an excellent FOM.

**IV. CONCLUSIONS**

In this study, a CMOS circulator and band-selection N path balun-LNA with RF SIC circuits were proposed and designed using a 65 nm CMOS technology. The designed CMOS circulator achieved an RX IL of 2.2 dB and a TX IL of 2.3 dB. The circulator and N-path balun-LNA with RF SIC circuits can achieve a total NF of 6.6 dB, an OB blocker rejection of more than 30 dB, and a total SIC of 58 dB for the CHBW of 20 MHz at 700 MHz. The proposed CMOS circulator and N-path balun-LNA with RF SIC circuits can provide antenna interface SIC and RF SIC, and enhance the blocker tolerance of the RX for advanced IBFD transceivers.

**Table 1.** Performance summaries and comparison with previous state-of-the-art works

| References | RFIC'20 [17] | JSSC'17 [18] | JSSC'15 [19] | ISSCC'17 [20] | ISSCC'19 [21] | RFIC'23 [22] | This Work* |
|---|---|---|---|---|---|---|---|
| Configuration | LNTA + RF/BB SIC + Mixer + TIA | Cir. + LNTA + Mixer + TIA + BB SIC | LNTA + RF SIC + Mixer + TIA | LNA + RF/BB SIC + Mixer + TIA | Cir. + Mixer + BB SIC + TIA | LNTA + RF/BB SIC + Mixer + TIA | Cir+ *N*-path balun-LNA+RF SIC |
| SIC Topology | Time-domain | Amp.&phase-based | Freq-domain | Time-domain | Time-domain | Time-domain | Time-domain |
| Process | 65nm CMOS | 40nm CMOS | 65nm CMOS | 40nm CMOS | 65nm CMOS | 65nm CMOS | 65nm CMOS |
| Frequency[GHz] | 0.1-1 | 0.6-0.8 | 0.8-1.4 | 1.7-2.2 | 2.2 | 0.1-1 | 0.6-1 |
| #of Taps(domain) | 7(RF)+7(BB) | 1(BB) | 2(RF) | 5(RF)+14(BB) | 5(BB) | 8(RF)+8(BB) | 5(RF) |
| SIC/Bandwidth @Frequency | 30dB/20MHz @738MHz | 22dB/12MHz @750MHz | 20dB/25MHz @1.37GHz | 50dB/42MHz @1.9GHz | 30dB/20MHz @2.2GHz | 27dB/160MHz @720MHz | 58dB/20MHz @700MHz |
| Gain [dB] | 15-38 (RFXE) | 42 (Cir. + RFXE) | 27-42 (RFXE) | 20-36 (RFXE) | 30 (Cir. + RFXE) | 15-40 (RFXE) | 17 (Cir. + LNA) |
| OB Blocker Rejection (dB) | NO | NO | NO | NO | NO | NO | YES(30**) |
| NF [dB] | 5.3 | 5.0 | 4.8 | 4.0 | 11.2 | 4.1 | 6.6 |
| Pdc [mW] | 32 | 30 | 44-91 per tap* | 11.5 | 46 | 22 | 14 |
| Area [mm] | 5.15 | 1.4 | 4.8 | 3.5 | 5.6 | 10.9 | 1.61 |
| FOM [dB] | 14.3 | 4 | 2.6 | 33.4 | 9.5 | 20.4 | 42.5* |

* Simulation result.
** at 100 MHz offset

## ACKNOWLEDGMENTS

This work was supported by the National Research Foundation of Korea(NRF) grant funded by the Korea government(MSIT) (No. 2023R1A2C1003227 and RS 2023-00221494). The chip fabrication and EDA tool were supported by the IC Design Education Center (IDEC), South Korea.

## REFERENCES

*[1] D. Bharadia et al., "Full duplex radios," in Proc. ACM SIGCOMM, 2013, pp. 375-386.*

*[2] A. Sabharwal et al., "In-band full-duplex wireless:Challenges and opportunities," IEEE J. Sel. Areas Commun., vol. 32, no. 9, pp. 1637-1652, Sep. 2014.*

*[3] A. Nagulu et al., "Ultra compact, ultra wideband,DC-1GHz CMOS circulator based on quasielectrostatic wave propagation in commutated switched capacitor networks," in Proc. IEEE RadioFreq. Integr. Circuits Symp. (RFIC), Jun., 2020, pp.55-58.*

*[4] A. Nagulu et al., "Multi-watt, 1-GHz CMOScirculator based on switched-capacitor clock boosting," IEEE J. Solid-State Circuits, vol. 55, no.12, pp. 3308-3321, Dec. 2020.*

*[5] A. Ruffino et al., "A wideband low-powercryogenic CMOS circulator for quantum applications," IEEE J. Solid-State Circuits, vol. 55,no. 5, pp. 1224-1238, May 2020.*

*[6] Y. Cao et al., "An integrated full-duplex/FDDduplexer and receiver achieving 100MHz bandwidth 58dB/48dB self-interference suppressionusing hybrid-analog-digital autonomous adaptationloops," in Proc. IEEE MTT-S InternationalMicrowave Symposium, 2020, pp. 1203-1206.*

*[7] M. Elkholy et al., "Low-loss integrated passiveCMOS electrical balance duplexers with singleended LNA," IEEE Trans. Microw. TheoryTechn., vol. 64, no. 5, pp. 1544-1559, May 2016.*

*[8] C. Wang et al., "A 0.5-4GHz full-duplex receiverwith multi-domain self-interference cancellation using capacitor stacking based second-order delaycells in RF canceller," in Proc. IEEE Radio Freq. Integr. Circuits Symp. (RFIC), Jun., 2022, pp. 259-262.*

*[9] R. Palaniappan et al., "A spectral shaper based two tap RF self-interference canceller for full-duplexradios," in Proc. IEEE MTT-S InternationalMicrowave Symposium 2019, pp. 614-617.*

*[10] H. Zhao et al., "Performance analysis of RF selfinterference cancellation in broadband fsystems," in Proc. IEEE International Conferenceon Communications Workshops, Kuala Lumpur, 2016, pp. 175-179.*
*[11] Y. Cao and J. Zhou, "Integrated self-adaptive andpower-scalable wideband interference cancellationfor full-duplex MIMO wireless," IEEE J. SolidState Circuits, vol. 55, no. 11, pp. 2984-2996, Nov.2020.*
*[12] M. Dastjerdi et al., "Analysis and design of a fullduplex two-element MIMO circulator-receiver withhigh TX power handling exploiting MIMO RF andshared-delay baseband self-interference cancellation,"IEEE J. Solid-State Circuits, vol. 54, no. 12, pp.3525-3540, Dec. 2019.*
*[13] I. Roberts et al., "Millimeter-wave full duplexradios: New challenges and techniques," IEEE Wireless Commun., vol. 28, no. 1, pp. 36-43, Feb.2021.*
*[14] N. Reiskarimian and H. Krishnaswamy, "Magneticfree non-reciprocity based on staggered commutation," in Nature Commun., vol 7, no. 4, p.11217, 2016.*
*[15] A. Nagulu et al., "Nonreciprocal components basedon switched transmission lines," IEEE Trans. Microw. Theory Techn., vol. 66, no. 11, pp. 4706-4725, Nov. 2018.*
*[16] D. Shin et al., "A blocker-tolerant receiver frontend employing dual-band N-path balun-LNA for 5G new radio cellular applications," IEEE Trans.Microw. Theory Techn., vol. 70, no. 3, pp. 1715-1724, March 2022.*
*[17] A. Nagulu et al., "A full-duplex receiver leveragingmultiphase switched-capacitor-delay based multi domain FIR filter cancelers," in Proc. IEEE RadioFreq. Integr. Circuits Symp. (RFIC), Jun., 2020, pp.43-46.*
*[18] N. Reiskarimian et al., "A CMOS passive LPTVnonmagnetic circulator and its application in a fullduplex receiver," IEEE J. Solid-State Circuits, vol.52, no. 5, pp. 1358-1372, May 2017.*
*[19] J. Zhou et al., "Integrated wideband selfinterference cancellation in the RF domain for FDD and full-duplex wireless," IEEE J. Solid-StateCircuits, vol. 50, no. 12, pp. 3015-3031, Dec. 2015.*
*[20] T. Zhang et al., "A 1.7-to-2.2GHz full-duplextransceiver system with >50dB self-interference cancellation over 42MHz bandwidth," in Proc.IEEE Int. Solid-State Circuits Conf, 2017, pp. 314-315.*
*[21] M. Dastjerdi et al., "Full-duplex 2×2 MIMOcirculator-receiver with high TX power handling exploiting MIMO RF and shared-delay basebandself-interference cancellation," in Proc. IEEE Int. Solid-State Circuits Conf, 2019, pp. 448-450.*
*[22] S. Garimella et al., "Frequency-domain equalization-based full-duplex receiver withpassive-frequency-shifting N-path filters achieving>53 dB SI suppression across 160 MHz BW," in Proc. IEEE Radio Freq. Integr. Circuits Symp.(RFIC), Jun., 2023, pp. 225-228.*
*[23] T. Chen et al., "A survey and quantitativeevaluation of integrated circuit-based antenna Interfaces and self-interference cancellers for fullduplex," IEEE Open Journal of theCommunications Society, vol. 2, pp. 1753-1776,2021.*

Seokwon Lee received the B. S. degree in Department of Electronics Engineering, Kangwon National University, Chuncheon, Korea, in 2023. He is currently working toward the M.S. degree in Department of Electronics Engineering, Kangwon National University, Chuncheon, Korea. His research interests include CMOS mmWave/RF/analog integrated circuits and RF system design for wireless communications.

Yonghwan Lee received the B. S. degree in Department of Electronics Engineering, Kangwon National University, Chuncheon, Korea, in 2023. He is currently working toward the M.S. degree in Department of Electronics Engineering, Kangwon National University, Chuncheon, Korea. His research interests include CMOS mmWave/RF/analog integrated circuits and RF system design for wireless communications

Chanhee Cho received the B. S. degree in Department of Electronics Engineering, Kangwon National University, Chuncheon, Korea, in 2023. He is currently working toward the M.S. degree in Department of Electronics Engineering, Kangwon National University, Chuncheon, Korea. His research interests include CMOS mmWave/RF/analog integrated circuits and RF system design for wireless communications.

Kuduck Kwon received the B.S. and Ph.D. degrees in Electrical Engineering and Computer Science from Korea Advanced Institute of Science and Technology (KAIST), in Daejeon, Korea, in 2004 and 2009, respectively. His doctoral research concerned digital TV tuners and dedicated short-range communication (DSRC) systems. From 2009 to 2010, he was a Post-Doctoral Researcher with KAIST, where he studied a surface acoustic wave (SAW)-less receiver architectures and developed 5.8GHz RF transceivers for DSRC applications. From 2010 to 2014, he was a Senior Engineer with Samsung Electronics Co. LTD., Suwon, South Korea, where he has been involved with studies of the SAW-less software-defined receivers and development of CMOS transceivers for 2G/3G/4G cellular applications and receivers for universal silicon tuners. In 2014, he joined the Department of Electronics Engineering, Kangwon National University, Chuncheon, South Korea, where he is currently a Professor. His research interests include CMOS mmWave/RF/analog integrated circuits and RF system design for wireless communications

# Instructions for Authors

**Essentials for Publishing in this Journal**

1 Submitted articles should not have been previously published or be currently under consideration for publication elsewhere.

2 Conference papers may only be submitted if the paper has been completely re-written (taken to mean more than 50%) and the author has cleared any necessary permission with the copyright owner if it has been previously copyrighted.

3 All our articles are refereed through a double-blind process.

4 All authors must declare they have read and agreed to the content of the submitted article and must sign a declaration correspond to the originality of the article.

**Submission Process**

All articles for this journal must be submitted using our online submissions system. http://enrichedpub.com/ . Please use the Submit Your Article link in the Author Service area.

-

**Manuscript Guidelines**

The instructions to authors about the article preparation for publication in the Manuscripts are submitted online, through the e-Ur (Electronic editing) system, developed by **Enriched Publications Pvt. Ltd**. The article should contain the abstract with keywords, introduction, body, conclusion, references and the summary in English language (without heading and subheading enumeration). The article length should not exceed 16 pages of A4 paper format.

**Title**

The title should be informative. It is in both Journal's and author's best interest to use terms suitable. For indexing and word search. If there are no such terms in the title, the author is strongly advised to add a subtitle. The title should be given in English as well. The titles precede the abstract and the summary in an appropriate language.

**Letterhead Title**

The letterhead title is given at a top of each page for easier identification of article copies in an Electronic form in particular. It contains the author's surname and first name initial .article title, journal title and collation (year, volume, and issue, first and last page). The journal and article titles can be given in a shortened form.

**Author's Name**

Full name(s) of author(s) should be used. It is advisable to give the middle initial. Names are given in their original form.

**Contact Details**

The postal address or the e-mail address of the author (usually of the first one if there are more Authors) is given in the footnote at the bottom of the first page.

**Type of Articles**

Classification of articles is a duty of the editorial staff and is of special importance. Referees and the members of the editorial staff, or section editors, can propose a category, but the editor-in-chief has the sole responsibility for their classification. Journal articles are classified as follows:

**Scientific articles:**

1. Original scientific paper (giving the previously unpublished results of the author's own research based on management methods).

2. Survey paper (giving an original, detailed and critical view of a research problem or an area to which the author has made a contribution visible through his self-citation);

3. Short or preliminary communication (original management paper of full format but of a smaller extent or of a preliminary character);

4. Scientific critique or forum (discussion on a particular scientific topic, based exclusively on management argumentation) and commentaries. Exceptionally, in particular areas, a scientific paper in the Journal can be in a form of a monograph or a critical edition of scientific data (historical, archival, lexicographic, bibliographic, data survey, etc.) which were unknown or hardly accessible for scientific research.

**Professional articles:**

1. Professional paper (contribution offering experience useful for improvement of professional practice but not necessarily based on scientific methods);
2. Informative contribution (editorial, commentary, etc.);
3. Review (of a book, software, case study, scientific event, etc.)

**Language**

The article should be in English. The grammar and style of the article should be of good quality. The systematized text should be without abbreviations (except standard ones). All measurements must be in SI units. The sequence of formulae is denoted in Arabic numerals in parentheses on the right-hand side.

**Abstract and Summary**

An abstract is a concise informative presentation of the article content for fast and accurate Evaluation of its relevance. It is both in the Editorial Office's and the author's best interest for an abstract to contain terms often used for indexing and article search. The abstract describes the purpose of the study and the methods, outlines the findings and state the conclusions. A 100- to 250-Word abstract should be placed between the title and the keywords with the body text to follow. Besides an abstract are advised to have a summary in English, at the end of the article, after the Reference list. The summary should be structured and long up to 1/10 of the article length (it is more extensive than the abstract).

**Keywords**

Keywords are terms or phrases showing adequately the article content for indexing and search purposes. They should be allocated heaving in mind widely accepted international sources (index, dictionary or thesaurus), such as the Web of Science keyword list for science in general. The higher their usage frequency is the better. Up to 10 keywords immediately follow the abstract and the summary, in respective languages.

**Acknowledgements**

The name and the number of the project or programmed within which the article was realized is given in a separate note at the bottom of the first page together with the name of the institution which financially supported the project or programmed.

**Tables and Illustrations**

All the captions should be in the original language as well as in English, together with the texts in illustrations if possible. Tables are typed in the same style as the text and are denoted by numerals at the top. Photographs and drawings, placed appropriately in the text, should be clear, precise and suitable for reproduction. Drawings should be created in Word or Corel.

**Citation in the Text**

Citation in the text must be uniform. When citing references in the text, use the reference number set in square brackets from the Reference list at the end of the article.

**Footnotes**

Footnotes are given at the bottom of the page with the text they refer to. They can contain less relevant details, additional explanations or used sources (e.g. scientific material, manuals). They cannot replace the cited literature.
The article should be accompanied with a cover letter with the information about the author(s): surname, middle initial, first name, and citizen personal number, rank, title, e-mail address, and affiliation address, home address including municipality, phone number in the office and at home (or a mobile phone number). The cover letter should state the type of the article and tell which illustrations are original and which are not.

Notes: